



Monitoring the Greater Agulhas Current With AIS Data Information

Clément Le Goff, Brahim Boussidi, Alexei Mironov, Yann Guichoux, Yicun Zhen, Pierre Tandeo, Simon Gueguen, Bertrand Chapron

► To cite this version:

Clément Le Goff, Brahim Boussidi, Alexei Mironov, Yann Guichoux, Yicun Zhen, et al.. Monitoring the Greater Agulhas Current With AIS Data Information. *Journal of Geophysical Research. Oceans*, 2021, 126 (5), pp.e2021JC017228. 10.1029/2021jc017228 . hal-03227798

HAL Id: hal-03227798

<https://hal.science/hal-03227798>

Submitted on 17 May 2021

HAL is a multi-disciplinary open access archive for the deposit and dissemination of scientific research documents, whether they are published or not. The documents may come from teaching and research institutions in France or abroad, or from public or private research centers.

L'archive ouverte pluridisciplinaire **HAL**, est destinée au dépôt et à la diffusion de documents scientifiques de niveau recherche, publiés ou non, émanant des établissements d'enseignement et de recherche français ou étrangers, des laboratoires publics ou privés.

Key Points:

- The high density of vessel traffic and associated Automatic Identification System messages provide means to derive the oceanic surface current
- An Helmholtz-Hodge decomposition of the optimally interpolated oceanic surface current field is performed
- In the core of the Greater Agulhas Current, analysis confirms that interpolated altimeter-derived estimates largely underestimate actual surface current velocities

Supporting Information:

Supporting Information may be found in the online version of this article.

Correspondence to:

C. Le Goff,
clement.legoff@e-odyn.com

Citation:

Le Goff, C., Boussidi, B., Mironov, A., Guichoux, Y., Zhen, Y., Tandeo, P., et al. (2021). Monitoring the greater Agulhas Current with AIS data information.

Journal of Geophysical Research: Oceans, 126, e2021JC017228. <https://doi.org/10.1029/2021JC017228>

Received 28 JAN 2021

Accepted 23 APR 2021

Monitoring the Greater Agulhas Current With AIS Data Information

Clément Le Goff¹ , Brahim Boussidi¹ , Alexei Mironov¹, Yann Guichoux¹, Yicun Zhen² , Pierre Tandeo² , Simon Gueguen³, and Bertrand Chapron⁴ 

¹eOdyn Brest, Plouzané, France, ²IMT Atlantique, Brest, Plouzané, France, ³Hytech-Imaging Brest, Plouzané, France, ⁴Ifremer LOPS Brest, Plouzané, France

Abstract Over the core region of the Agulhas Current, new estimations of ocean surface velocities are reported using the increasing data set from the Automatic Identification System (AIS), initially designed to monitor vessel traffic. A two-step strategy is suggested. A first guess is evaluated from the collective behavior of vessels for a given space-time interval. Individual vessel trajectories are then re-analyzed and interpolated. Applied during year 2016, these ocean surface current estimates are demonstrated to well determine the intensity of surface currents. The improved spatial resolution helps the decomposition of the optimally interpolated surface current vector field between irrotational $\approx 80\%$ – 90% and divergence-free components $\approx 10\%$ – 20% , for example, Helmholtz-Hodge decomposition. Comparisons are performed between in situ drifting-buoys and represent up to 25% gain in respect of the altimetry gridded current (for the meridional component). Others comparisons with data collected during the Agulhas Current Time-series experiment, as well as with the mean Doppler-derived surface currents obtained from satellite synthetic aperture radar measurements also reveal a significant benefit of using the AIS derived estimates. Comparisons with the Sea Surface Temperature from MODIS sensors confirm the occurrence of meandering events for the current path. For the Agulhas Current region, the high density of vessel traffic can provide new means to study and monitor intense upper ocean currents with more detailed resolution and precision.

Plain Language Summary Today, for security reasons, merchant ships transmit location, speed, heading and course-over-ground information through the Automatic Identification System (AIS). These messages are a new source of information to complement ocean surface current measurements. In this study, the intense traffic off the South African coast can result in a selection of more than 150 ships per day. Daily analyses and correlations are reported and illustrate links with observed changes in sea surface temperature. In view of the existing need to establish a more comprehensive monitoring system for the Agulhas Current, these results encourage the systematic usage of the increasingly available amount of AIS data as complementary to traditional in situ and altimeter measurements for routine quantitative monitoring of heat and mass transport in this region.

1. Introduction

Measurements of powerful, complex and highly variable upper ocean surface currents are fundamental to better understand ocean circulation and air-sea interactions influencing the Earth system on different scales (e.g., Caesar et al., 2021), from very short wind waves to entire weather systems. Within an evolving Earth climate, wind-driven ocean surface currents are sure to vary, leading to different patterns of sea surface temperature and salinity with profound consequences for ecosystems such as the loss of coral through bleaching. The latter are also impacted by the accumulation of marine plastics in the ecosystem and along the shore. Anomalous ocean surface currents can also emerge, further complicating all these aspects, modulating sea level at regional scales with strong impacts on local ocean circulation. At these local scales, divergence and convergence of the ocean surface currents will control vertical exchanges between the ocean surface, exposed to the atmosphere, and the interior ocean at depth. Today, only for large spatial (100–200 km) and temporal scales (10–30 days), can we use radar altimeters to depict and quantify large coherent upper ocean structures with signatures extending down, several hundreds of meters into the ocean interior.

Before the altimetry era, ocean surface current estimates were based on the logs of both military and merchant ships (Richardson & McKee, 1984; Richardson & Reverdin, 1987; Richardson & Walsh, 1986). Indeed, in the presence of intense currents, ships may be pushed off-course and their speed be modified. Subtracting the predicted vector, based on dead reckoning, from the vector representing the ship's actual speed and direction, surface current estimates can then be derived. This method may have lacked accurate positioning and time sampling. However, precision in geo-positioning has been largely improved. Moreover, today, merchant ships systematically transmit their position, bearing and speed through Automatic Identification System (AIS) messages, increasing the number of estimates. Early studies have shown the relevance of using AIS information and ship trajectory analysis to estimate surface currents (Guichoux, 2015; van der Neut, 2016). Some comparisons between high-frequency radar (HFR) measurements and AIS-derived surface currents have shown excellent concordance, particularly over tidal currents in coastal regions. These first efforts also revealed capabilities to detect mesoscale structures such as eddies and filaments in the Sicily Channel, Italy (Guichoux et al., 2016). Inazu et al. (2018) also exploited AIS data messages to reveal the presence of a passing tsunami event, further demonstrating that associated AIS-derived currents quantitatively captured the speed of the tsunami's current. Accordingly, AIS data messages can thus provide opportune new sources of information to complement and improve current ocean observation systems.

In certain oceanic regions, that is, off the South African coast, marine traffic is so intense that data from more than 150 ships can be used each day. As discussed in the present paper, such a wealth of information can be combined with all available *a priori* surface current estimates, particularly those derived from satellite altimetry and drifting-buoys, in order to develop an improved spatio-temporal surface current monitoring system.

The present demonstration focuses on the northern part of the Agulhas Current, between 32°S and 36°S, where maritime traffic is most intense all year round. With a mean transport of about 70 Sverdrup (1 Sverdrup = $10^6 \text{ m}^3 \text{ s}^{-1}$), and surface current speeds, at times greater than 2 ms^{-1} , the Agulhas Current constitutes the strongest western boundary current of the Southern Hemisphere, if not of the world (Bryden et al., 2005). The flow along the eastern coast of South Africa is steered by, and essentially follows, the very steep continental shelf break. This strong and energetic Agulhas Current induces Ekman veering along its landward edge and favors the upwelling of cold and nutrient-rich water to the surface. In its northern branch, the Agulhas Current generally displays remarkably little variability. Still, one type of meander which often receives considerable attentions is the Natal Pulse phenomenon (Lutjeharms, 2007; Rouault & Penven, 2011). Natal Pulses are large meanders of the Agulhas Current which originate near the Natal Bight (29°S) and are thought to play an important part in the downstream variability of the Agulhas Current and the subsequent leakage of warm and salty Agulhas Current water into the Atlantic Ocean.

In its core part, commonly reported large surface velocities, up to 2 ms^{-1} , likely impact upon vessel trajectories. To note, such extreme values are generally not reported in interpolated gridded fields obtained from combined altimeter measurements. Besides inherent smoothing induced by the interpolation of sparse satellite measurements, this underestimation of current velocities may also be due to the presence of non-geostrophic components of the real current (Beal & Donohue, 2013; Krug et al., 2018). In addition, close to the shore, altimetry can suffer serious limitations due to factors such as land contamination, atmospheric errors or inaccuracies in the estimation of the mean dynamic topography (MDT), generally resulting in less precise data within 30 km of the coast.

In the present study we developed a methodology in two steps. The first consists in calculating a first guess of the oceanic surface current. As explained in Section 2, assuming that all vessels, within a given space-time interval, encounter the same sea surface conditions, a surface current estimate can be found as the solution of a linear system. However, this method suffers from large errors. We therefore filter the data using physical considerations regarding the variance of the different velocities associated to each vessel. This first method requires a substantial number of AIS messages from different vessels to converge. We consider this result our first guess. In the second step, we fill in the gaps inherent to this first method by returning to the vessels' individual data over time and interpolating their navigation characteristics. We then provide the associated currents along the vessel trajectories, correcting the first guess and project them on to a regular grid. We consider these fields our second guess. Finally, we applied an optimal interpolation to fulfill the

gaps of the regular grid. The improved spatial resolution helps the application of the Helmholtz-Hodge decomposition between rotational- and divergence-free components.

In situ and diverse remote sensing data, used for the validation of the derived surface current field are presented in Section 3. In Section 4, our new AIS-based estimates are compared to these different sources of information. Particular attention is paid to drawing comparisons with the Mean Dynamic Topography (MDT) and with the resulting mean geostrophic current in the area. More locally, analysis has also been conducted over a particular Altimeter track, intercepting in situ, long-term ACT measurements (Beal et al., 2015). Besides these long-term annual average comparisons, particular cases are considered, including a Natal pulse event. For the latter comparison, high-resolution satellite observations (Synthetic Aperture Radar, sea surface temperature, and ocean color) are used to provide concurrent information.

2. AIS Data and Processing Methods

2.1. AIS Messages and Drift Velocities

In the Agulhas current, marine traffic is particularly intense. In 2016, off the coast of Port Elisabeth, 23°E–29°E and 32°S–36°S, up to 1,000 vessels transmitted their AIS messages each day. Messages are obtained from ORBCOMM and gathered using satellites. These messages include static and dynamic information. The static information includes the MMSI (Maritime Mobile Service Identity), the ship's name and type, its length and its draft. The dynamic information includes longitude/latitude, speed over ground (SOG), course over ground (COG) and the ship's heading (true heading or TH). It must be noted that, the emission period of the AIS messages is around 10 s and the sampling rate of the data obtained from Satellite AIS is around a few minutes.

However, all messages may not be useful. Indeed, all vessels do not necessarily have a continuous course over ground, or are simply not in transit (e.g., fishing vessels). Thus, from the reported trajectories and speeds, only messages corresponding to vessels in transit were kept. To illustrate data availability, the mean daily number of AIS messages, per 0.125° square box, is shown in Figure 1a. We can clearly see that marine traffic follows the coast closely, at a maximal distance of around 100 km. At its peak intensity, the mean number of AIS data messages per grid cell and per day can be as high as 180 for approximately 15 vessels (Figures 1a and 1b).

As also illustrated in Figure 1, ships in transit generally follow straight lines between two way points. In the presence of sea surface currents, the true heading (direction pointed to by the vessel) then adjusts to best follow the prescribed route. The vocabulary and a diagram are presented in Figure 2. As a basic principle, the composition of the different velocity vectors is given by:

$$\overrightarrow{V_{Boat/Ground}} = \overrightarrow{V_{Boat/Sea}} + \overrightarrow{V_{Sea/Ground}} \quad (1)$$

$\overrightarrow{V_{Boat/Ground}}$ is measured using the ground distance traveled during a fixed time, with its associated magnitude (SOG) and direction (COG) provided in the AIS message. $\overrightarrow{V_{Boat/Sea}}$ is the vector velocity of the boat relative to the sea surface, with its associated direction (TH) also provided in the AIS message. The magnitude of $\overrightarrow{V_{Boat/Sea}}$ stays unknown. As such, $\overrightarrow{V_{Sea/Ground}}$ is a completely unknown oceanic surface current vector. By projection, in this case on the horizontal and vertical axes associated with the zonal and meridional velocity components, we obtain two equations and three unknown variables (i.e., direction and magnitude of the drift (oceanic current) and magnitude of the boat's speed relative to the sea):

$$\begin{cases} V_{sog}^* \sin(\varphi_{cog}^*) = V_{stw} \sin(\varphi_{th}^*) + u_{drift} & \text{(zonal)} \\ V_{sog}^* \cos(\varphi_{cog}^*) = V_{stw} \cos(\varphi_{th}^*) + v_{drift} & \text{(meridional)} \end{cases} \quad (2)$$

For each AIS data message, V_{sog} is the speed over ground, φ_{cog} the course over ground, V_{stw} the speed through water and φ_{th} the true heading of each ship considered. u_{drift} and v_{drift} represent the zonal and meridional components of the vessel drift which, in line with our hypothesis (explained hereafter), correspond to the ocean surface current u_{os} and v_{os} . As in Figure 2, the asterisk indicates variables obtained from the AIS messages.

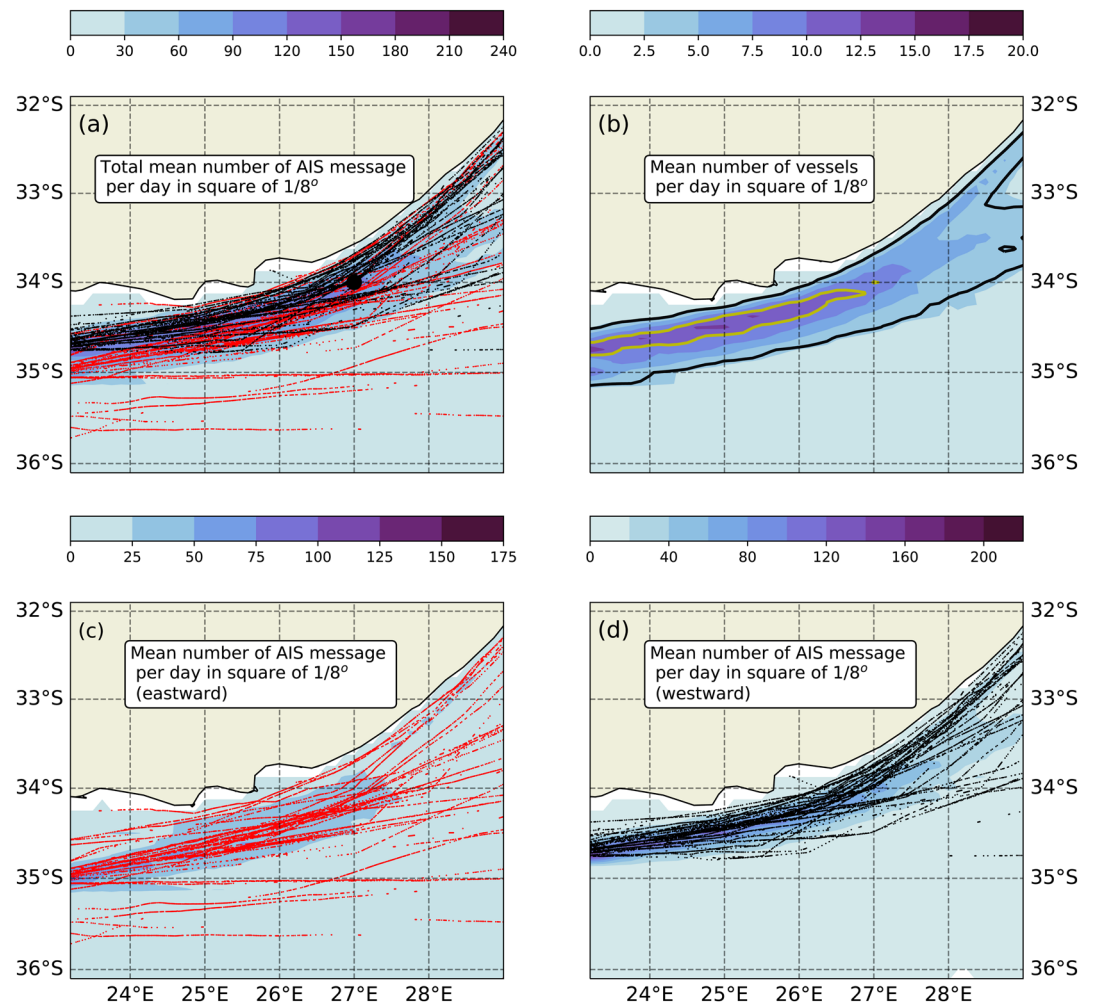


Figure 1. Mean daily number of AIS related messages in a grid of 0.125°. (a) Total number of AIS messages. (b) Total number of vessels. (c) Number of AIS messages related to Eastward bound vessels. Trajectories are represented by a red dot and correspond to a given day. (d) Same as (c) but for Westward bound vessels. Trajectories are represented in black. The dot corresponds to the location where maritime traffic and wind were analyzed (see Figure 4).

It is important to note that all basic assumptions are valid so long as the equation of motion of the vessel yields to $m \frac{dv}{dt} \approx 0$. This also helps with discarding stormy weather conditions or maneuvering operations. In Inazu et al. (2018), the characteristic time response of the vessel was estimated to be around 40–120 s. This timescale is small compared to the timescale of the oceanic surface current. For this reason, computing the oceanic current seems feasible as long as the motion of the vessel reaches a steady state, as we will further see.

2.2. Impact of the Wind—Leeway Drift

Wind directions in the Agulhas typically flip between SW and NE as shown in Figure 3a for the year 2016, in a region located near the longitude latitude point (27°, −34°). The wind data were obtained from the ECMWF ERA-Interim reanalysis product available at <http://apps.ecmwf.int/datasets/>. For the same area, the mean direction and the mean speed of the vessels in transit for both destinations (Indian or Atlantic Ocean) are reported in Figure 3b. The wind is likely to affect vessel speed through water by blowing either from the front or from behind. The vessel may thus accelerate or decelerate rather than being pushed off course (no lateral effect). Strong winds with an orientation perpendicular to the course of the boat could modify

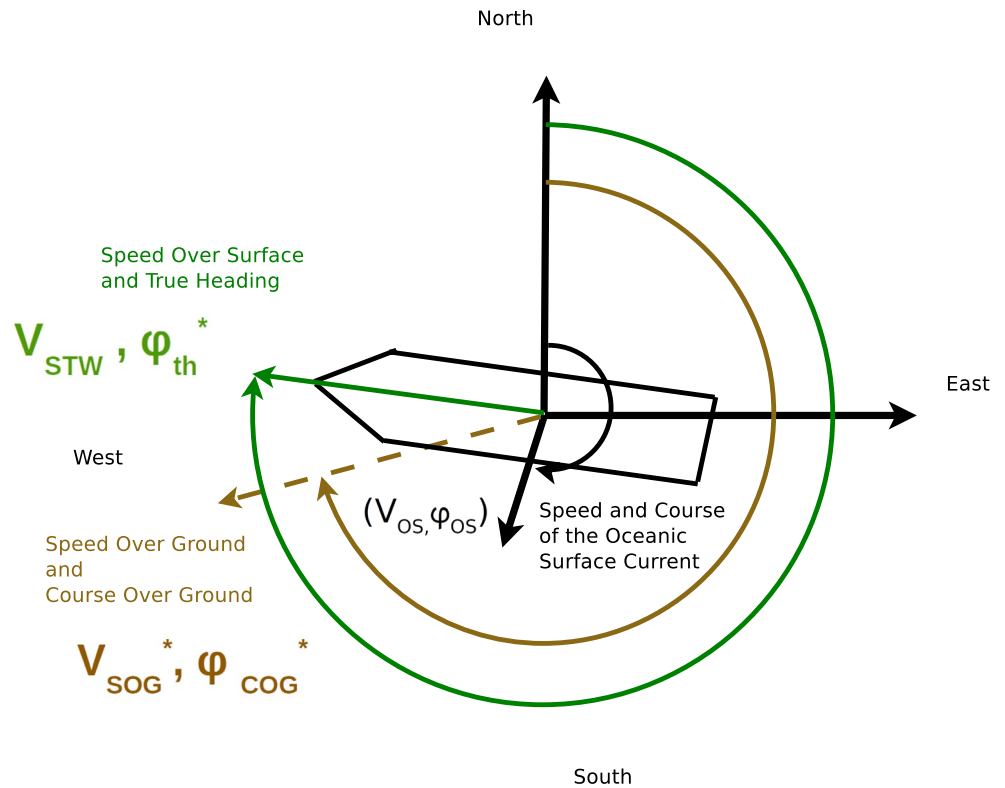


Figure 2. Measurement diagram and definitions. Variables with an asterisk are known and transmitted via the AIS message. The other variables are calculated. When projected over the zonal and meridional axes V_{os} and φ_{os} become u_{os} and v_{os} .

the true heading thus hindering surface current estimations. However, considering a standard boat, Richardson (1997) demonstrated that the wind-induced drift is small compared to that of the oceanic current. The leeway drift of a boat enduring complete lateral wind of magnitude 6 ms^{-1} would amount to around 3.5 cms^{-1} , only 0.6% of the wind's magnitude. The fact that the wind is not always lateral further weakens this percentage. Given the results of these analyses, the leeway drift is not considered in the present

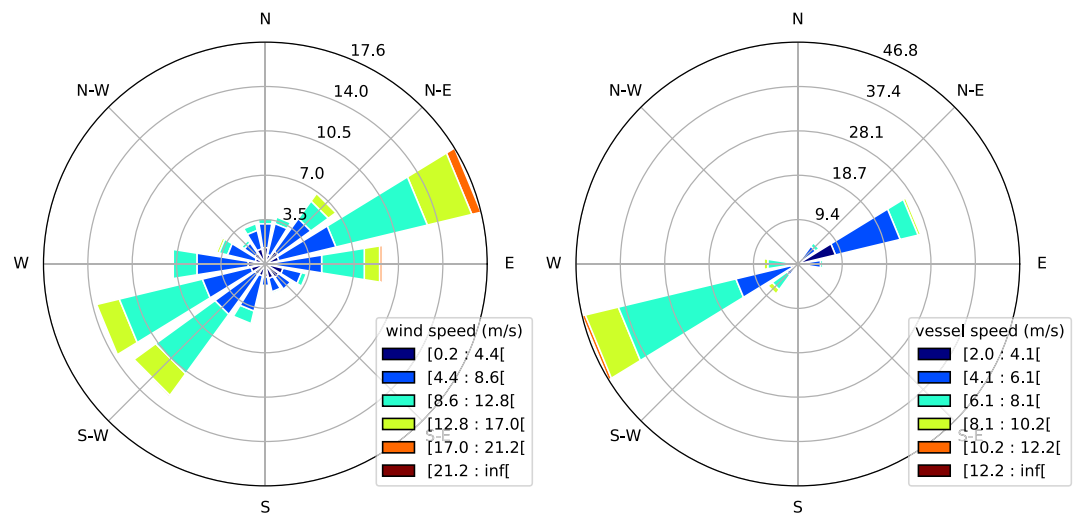


Figure 3. (a) ECMWF wind rose diagram at point (27°E, 34°S), located in the Agulhas current. (b) Wind rose diagram showing the mean direction and speed of vessels traveling with the flow (South-westerly) and against the flow (North-easterly) for all vessels located inside a square 0.5° around coordinates (27°E, 34°S).

evaluation in the Agulhas region. Nevertheless, the wind does play a crucial role in vessel behavior in an indirect manner, as further explained below.

2.3. First Guess of the Surface Current

Vessels and associated AIS messages, are first considered to be in homogeneous surface conditions in both space and time. Given that solving the linear system requires a sufficient amount of data, the AIS messages are aggregated within three different spatio-temporal boxes. Figure 1b shows black and yellow contours corresponding to densities of 3 and 10 vessels per day, per $1/8^\circ$ square box, respectively. For densities superior to 10, we considered cells of $1/8^\circ \times 1/8^\circ$ over a 1-day period. For densities between 3 and 10, we changed this time interval to a 3-day period and for densities inferior to 3, we considered cells of $1/4^\circ \times 1/4^\circ$ within a 5-day period. For each AIS message, we have two equations and three unknowns, the magnitude of V_{stw} and the two current components. For n AIS messages, we therefore have $2n$ equations. However, using the space-time homogeneity assumption, this leaves only $n + 2$ unknowns to be solved. The following system is thus considered:

$$\begin{cases} V_{sog1}^* \sin(\varphi_{cog1}^*) = V_{stw1} \sin(\varphi_{th1}^*) & + u_{os} \\ V_{sog1}^* \cos(\varphi_{cog1}^*) = V_{stw1} \cos(\varphi_{th1}^*) & + v_{os} \\ \vdots & \vdots \\ V_{sogn}^* \sin(\varphi_{cogn}^*) = V_{stw_n} \sin(\varphi_{th_n}^*) & + u_{os} \\ V_{sogn}^* \cos(\varphi_{cogn}^*) = V_{stw_n} \cos(\varphi_{th_n}^*) & + v_{os} \end{cases} \quad (3)$$

Although seemingly overdetermined, this system still requires a significant number of AIS messages and suffers from almost three sources of error. To illustrate the main source of error, we can write the equation to be solved as follows:

$$Ax = b \quad (4)$$

with A being the matrix to invert in order to calculate the oceanic surface current such as:

$$A = \begin{pmatrix} 1 & 0 & \sin(\varphi_{th1}^*) & 0 & \dots & 0 \\ 0 & 1 & \cos(\varphi_{th1}^*) & 0 & \dots & 0 \\ \vdots & \vdots & & & \ddots & \\ 1 & 0 & 0 & \dots & 0 & \sin(\varphi_{th_n}^*) \\ 0 & 1 & 0 & \dots & 0 & \cos(\varphi_{th_n}^*) \end{pmatrix}, x = \begin{pmatrix} u_{os} \\ v_{os} \\ V_{stw1} \\ \vdots \\ V_{stw_n} \end{pmatrix}, b = \begin{pmatrix} V_{sog1}^* \sin(\varphi_{cog1}^*) \\ V_{sog1}^* \cos(\varphi_{cog1}^*) \\ \vdots \\ V_{sogn}^* \sin(\varphi_{cogn}^*) \\ V_{sogn}^* \cos(\varphi_{cogn}^*) \end{pmatrix} \quad (5)$$

where A and b correspond to the observations and x corresponds to the unknowns. Considering matrix A, one may note a particular case in which all the vessel headings (φ_{th_i}) are similar or equal. Mathematically this would correspond to a badly conditioned matrix and a solution to this system would be difficult to obtain. In practice, it would correspond to an area where all the vessels have approximately the same true heading. This situation is clearly illustrated in Figures 1c and 1d where the densities of the AIS messages from vessels going westwards and vessels going eastwards are plotted separately. It may be noted that in the north-eastern part, there is no preferred maritime route. This leads to diverse headings for the different vessels and facilitates the calculation of the current by inverting the linear system 3. Nevertheless, considering the south-western part, traffic is far more organized and we can easily identify three lanes of traffic. Clearly, the diversity of vessel headings is small in these areas and a solution of the system 3 may lead to considerable errors. More detailed explanations are provided in the Supporting Information S1. For this same reason, we only invert the system when a minimum of three vessels are present inside our spatio-temporal cell. Indeed, if such is the case, the redundancy of the heading concerning a unique vessel is high and does not allow for a successful inversion of the system.

Although a badly conditioned matrix may be considered a major source of error in our investigation, additional sources are traffic density and bad weather conditions. Stormy weather impacts the fluctuation of the variables provided by the AIS data messages, preventing the system from finding a correct solution.

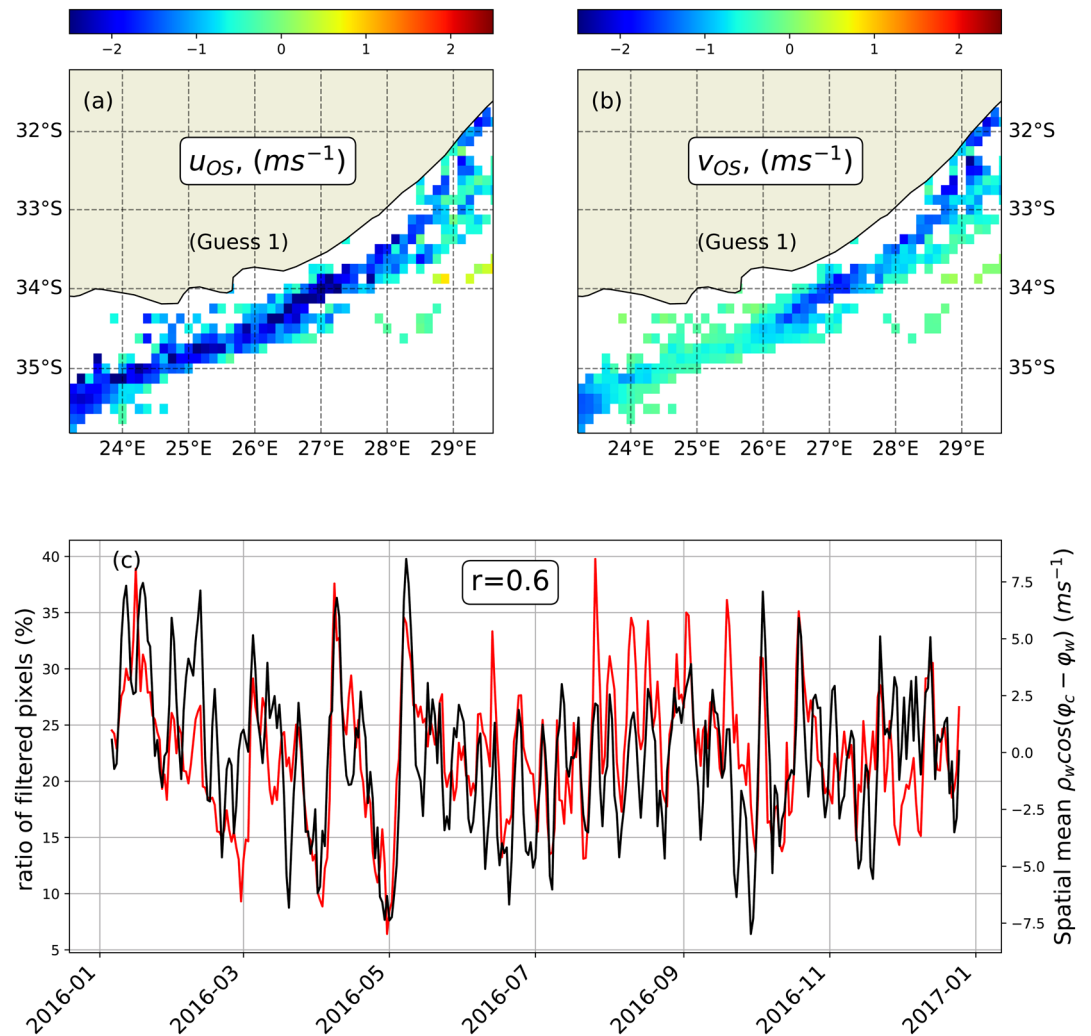


Figure 4. Maps of the filtered oceanic surface current for (a) the zonal component and (b) the meridional component for January 16, 2016. (c) In black, percentage of the number of filtered boxes over the total number of boxes as a function of time (day). In red, the mean scalar product of the wind and geostrophic ocean current as a function of time (day).

2.4. Second Guess of the Surface Current

Direct calculation of surface currents thus leads to considerable errors. An example of the direct estimates found by solving the linear system and explanations are given in the Supporting Information S1. To improve the results, we used additional information regarding the speed through water (V_{stw}), also obtained when solving the linear system. The idea of this filtering technique is to consider each result associated to each spatio-temporal box (pixel) and to assign a binary quality index to it. The technical details are given in Supporting Information S2.

Figure 4 shows the pixels with a good quality index, the maps (a) and (b) correspond to the zonal and the meridional oceanic surface components. Figure 4c indicates the amount of points retained, that is, the ratio between the number of pixels with a good quality index over the total number of pixels for which a calculation was carried out. By repeating this operation for each day, we obtained a corresponding time-series. To qualify the main variability of the signal we calculated the mean magnitude of the wind in the direction of the geostrophic current (averaged over the whole domain) (see Section 3.1.1). In polar coordinates this term corresponds to $\rho_w \cos(\varphi_c - \varphi_w)$, ρ_w being the magnitude of the wind, φ_c and φ_w being the direction of the current and the wind respectively. In Figure 4c, we clearly note the significant correlation between the

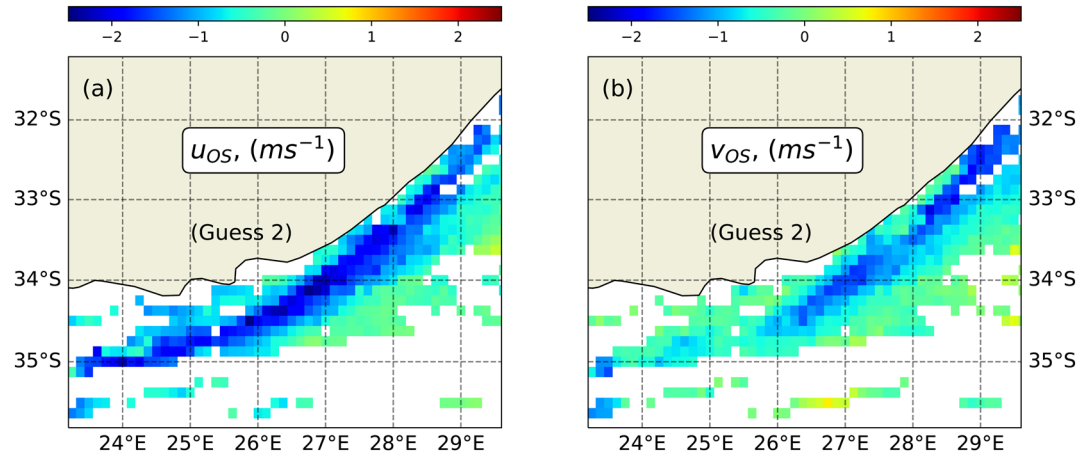


Figure 5. Second guess of the zonal (a) and meridional (b) components of the oceanic surface current for January 16, 2016.

two signals $r = 0.6$. This result indicates that our filter, explained above, successfully discards environmental conditions, such as stormy weather, that interact with the current. Indeed, the situation in which the wind blows against the current is known to cause very difficult sea conditions for vessels and quite logically prevents calculation of the oceanic current. Other similar sources of error may come from the refraction of the waves by the current, leading to substantial amplification of the significant wave height (Ardhuin et al., 2017; Kudryavtsev et al., 2017a; Quilfen & Chapron, 2018; Quilfen et al., 2018). In these specific cases, the hypothesis that vessels are in homogeneous surface conditions, in both space and time, is no longer valid. Instead of counteracting the oceanic surface current by adjusting their heading, vessels tend to slow down and maneuver in order to keep their heading perpendicular to the dominant wave. This effect will be the subject of a future study as it may provide a powerful tool to analyze hazardous sea-states and could thus contribute to improving safety at sea.

A first guess of the oceanic surface current gathers information shared by the vessels within a given space-time interval. This method involves the aggregation of data, thus lowering the spatial and temporal resolution. Moreover, while our filtering technique based on the variance of the different speeds V_{sog} and V_{stw} of the vessels enables us to better discard outliers, one can easily observe on Figures 4a and 4b that the results and the corresponding maps still exhibit notable noise levels. To improve the first-guess estimates, the basic idea consists in regularizing and augmenting the spatio-temporal resolution using the time continuity of the vessels' speed through water. To do so, we consider the vessels along their entire journey and collect all their calculated speeds through water obtained by solving the system 3.

Having obtained the time-series of the speed through water, we then filter our results using the Empirical Mode Decomposition. For this, we only keep the trend of the EMD (Huang et al., 1998; Kopsinis & McLaughlin, 2009). From this filtered estimate of speed through water we then use the set of Equation 2 and calculate the zonal and meridional components of the oceanic surface current as follows:

$$\begin{cases} u_{os} = \mathcal{F}(V_{stw})\sin(\varphi_{TH}) - V_{sog}\sin(\varphi_{cog}) & \text{(Zonal Guess 2)} \\ v_{os} = \mathcal{F}(V_{stw})\cos(\varphi_{TH}) - V_{sog}\cos(\varphi_{cog}) & \text{(Meridional Guess 2)} \end{cases} \quad (6)$$

where $\mathcal{F}(V_{stw})$ represents the filter for the speed through water. Examples and more detailed explanations are given in the Supporting Information S3.

The results obtained from the second guess are illustrated in Figure 5 where the zonal (a) and the meridional (b) velocities are plotted on the map for the same day as for the first guess, that is, January 16, 2016. As expected, the global spatial coverage is higher as the individual information for each vessel is now used systematically to infer the oceanic surface current. As previously mentioned, this method is not accurate

every time and everywhere and, essentially, is incorrect when the wind blows against the current (Figure 5). Before projecting the estimates from the daily available vessels onto the same regular grid as done previously, we thus select the periods when the wind was not blowing against the current, that is, when $\rho_w \cos(\varphi_c - \varphi_w) > 0$. Where φ_c and φ_w are the direction of the current and wind and ρ_w is the wind magnitude.

2.5. Optimal Interpolation

Once a clean data set obtained for both the zonal and the meridional velocity components, we apply a classic optimal interpolation in order to smooth and map the results in space and time (Bretherton et al., 1976). The results of the interpolations are Gaussian, defined by their mean fields u_{os}^s , v_{os}^s , and associated covariance $P_{u_{os}}^s$, $P_{v_{os}}^s$. Here, the index s indicates the smoothing results (i.e., the interpolation using all available data along a given region and time period).

Optimal interpolation is a mathematical tool used to merge background information (x^b) from *a priori* knowledge, in this case, the annual average of the zonal and meridional current estimates and observations (y). The result of the optimal interpolation is Gaussian with a mean x^s and a covariance P^s given by:

$$\begin{aligned} x^s &= x^b + K(y - Hx^b), \\ P^s &= B - KHB, \\ \text{with the gain } K &= BH^T(HBH^T + R)^{-1}, \end{aligned} \quad (7)$$

where H is the observation operator, thus creating the link between the observation and the background. Here, H is the identity matrix.

The background B and observation R covariances defined in Equation 7 significantly impact the interpolation results and consequently must be estimated. These two covariances depend on important parameters: noise levels and spatio-temporal correlation lengths. Variograms are classic statistical tools used to estimate these parameters from available measurements (Tandeo et al., 2014). The variograms were calculated empirically in both space and time and results are shown in Figure 6. For a given δ_s (or δ_t), the empirical variogram of the zonal (or meridional) current is defined by the mean squared difference between all zonal currents (or all meridional currents), separated by the spatial distance δ_s (or the temporal distance δ_t). We then fitted the empirical variograms using an exponential spatio-temporal shape, defined by:

$$\gamma(\Delta_s, \Delta_t) = R + \sigma^2 \left(1 - \exp\left(-\frac{\Delta_s}{L}\right) \exp\left(-\frac{\Delta_t}{T}\right) \right) \quad (8)$$

where R corresponds to the observation error variance, σ^2 to the stationary variance of the process, L to the spatial correlation length, and T to the temporal correlation length. The exponential shape of the theoretical variogram is a simple and specific case of the Matern function, used for its good mathematical properties. The correlation lengths and variance parameters in Equation 8 are estimated using an optimization procedure, based on the minimization of the mean square error between the empirical and theoretical variograms. The fitted variograms using the formula given in Equation 8 are also shown in Figure 6. The variance parameters, for both zonal and meridional components of the current, are $R_u = 0.1$ and $R_v = 0.05$ for the observation variance, $\sigma_u = 0.4$ and $\sigma_v = 0.25$ for the stationary variance. The correlation lengths were equal for two components of the current, $L_u = L_v = 0.6^\circ$ for space, and $T_u = T_v = 20$ days for time. These correlation length values are consistent with those normally used in the interpolation of altimeter data (Le Traon et al., 1998).

The corresponding optimally interpolated fields of the zonal and meridional components of the oceanic current are presented in Figures 7a and 7b. The associated square root covariances $\sqrt{P_{u_{os}}^s}$, $\sqrt{P_{v_{os}}^s}$ are presented in Figures 7c and 7d. These terms can be considered estimates of the errors associated to optimal interpolation. Not surprisingly, we note that these maps are very similar to those of maritime traffic presented in Figure 1.

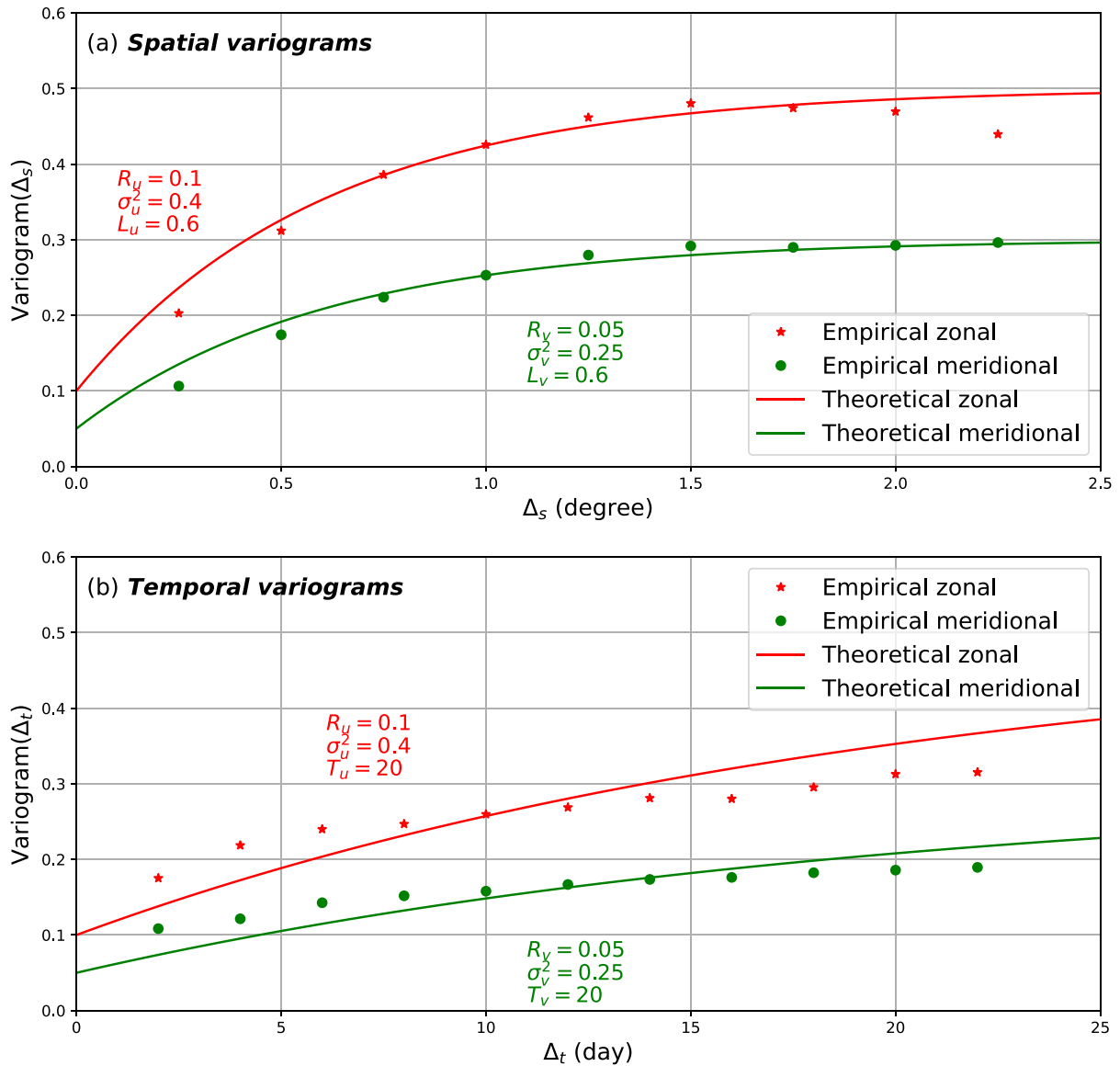


Figure 6. (a) Empirical and theoretical spacial variograms of the zonal and meridional current components. (b) Corresponding temporal variograms.

2.6. Helmholtz-Hodge Decomposition of the Optimally Interpolated Field

Oceanic currents are the result of different physical mechanisms at different scales. Among these are differences in sea level (Geostrophy balance), wind (Ekman transport) and waves (Stoke Drift) and so on. While a geostrophy balance leads to a divergent-free flow, this is generally not the case for the other mechanisms and their interactions. Moreover, ocean flow is always considered incompressible which means that the divergence obtained from the analysis of the oceanic surface flow must be related to the vertical motion of the ocean, and more generally to ageostrophic processes. In order to study and identify these different physical mechanisms, we can use the Helmholtz-Hodges decomposition, briefly described here. This decomposition describes the flow as the sum of rotation-free, divergent-free and harmonic vector fields. Considering a smooth vector field $\vec{\xi}$ as the result of the optimally interpolated fields then,

$$\vec{\xi} = \vec{r} + \vec{d} + \vec{h} \quad (9)$$

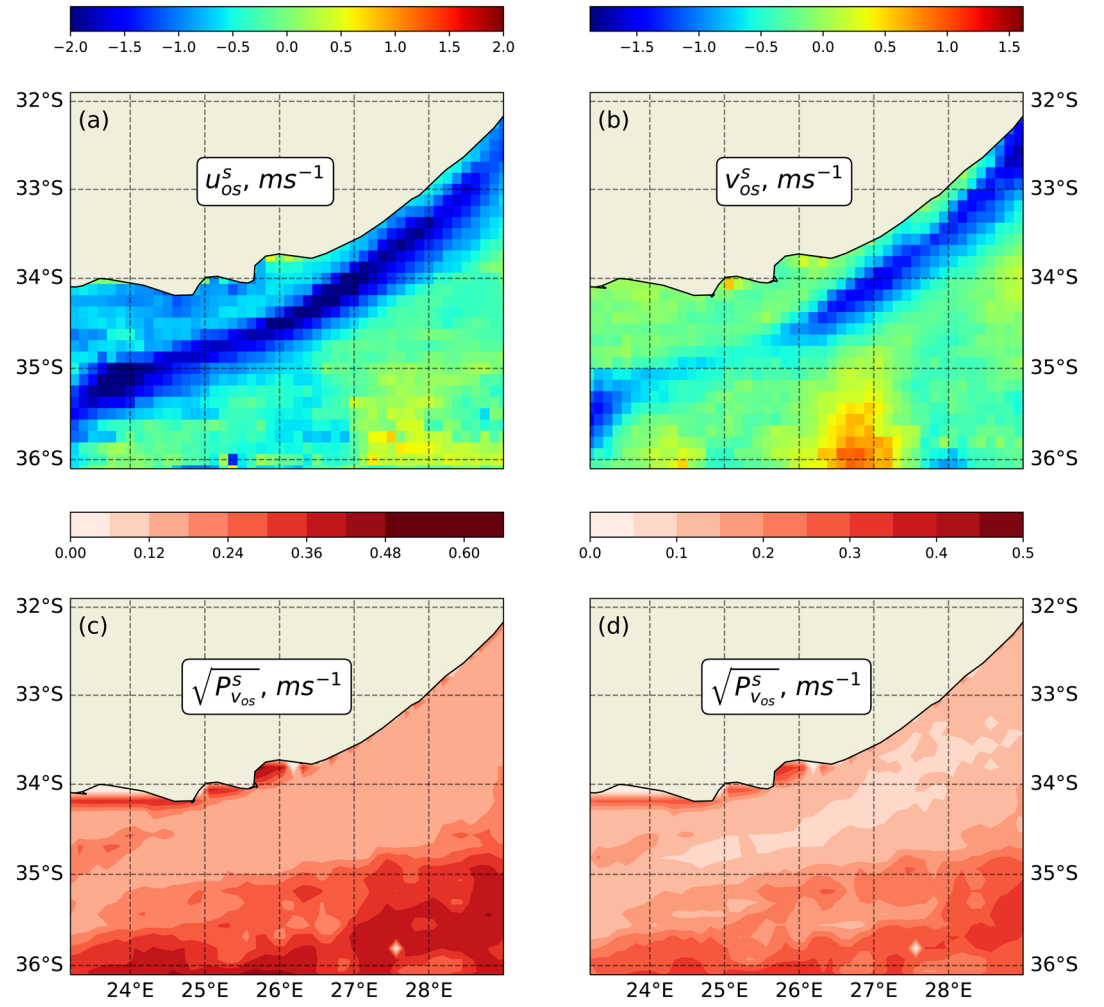


Figure 7. Zonal (a) and meridional (b) oceanic surface current components obtained from the optimal interpolation for January 16, 2016. (c) and (d) show the covariances associated to the zonal and meridional means respectively.

where \vec{r} is the divergent-free ($\nabla \cdot \vec{r} = 0$), \vec{d} is the rotation-free ($\nabla \times \vec{d} = 0$) and \vec{h} is harmonic ($\nabla \times \vec{h} = 0$ and $\nabla \cdot \vec{h} = 0$). This leads to the following equations:

$$\nabla \cdot \vec{d} = \nabla \cdot \vec{\xi} \quad (10)$$

$$\nabla \times \vec{r} = \nabla \times \vec{\xi} \quad (11)$$

When substituting $d = \nabla D$ and $\vec{r} = \nabla \times \vec{R}$ the above equations become two Poisson's equations. Nevertheless, the above system is under-specified, given that for any harmonic flow added to the solution, the resulting sum is still a solution. This raises the problem of the uniqueness of the solution when the domain is bound (in an infinite domain the harmonic flow disappears). Most related studies use the NP (Normal parallel) boundary conditions which forces the rotational (divergent) flow to be normal (parallel) to the boundaries. Here, we used the so-called Natural Helmholtz-Hodges Decomposition (nHHD) (Bhatia et al., 2014). The basic idea is to consider the domain under external and internal influences. As such, the rotational and divergent flows are under the internal influences (in the domain) and the harmonic flow is under the external influence (at the boundaries). An advantage of applying this method is the non-use of boundary conditions to obtain the uniqueness of the solution. The sole limitation of the nHHD is that it is not guaranteed to be L2-orthogonal between the divergent, d and the rotational, r flows. For visualization and analysis this prop-

erty is not required. Further details and explanations are provided in (Bhatia et al., 2014). The subscripts ξ , r , and d refer to the optimal velocity field, the divergent-free flow field and the rotational-free flow field.

3. Validation Data

3.1. Remote Sensing

3.1.1. Geostrophic Velocity Gridded Field and Along-Track Altimetry

The geostrophic velocities are derived from the altimeter products, using both the gridded geostrophic velocity and the Along-Track estimates.

For the gridded geostrophic velocity, we used the Sea Level Anomaly (SLA) obtained through the altimeter-gridded products, http://marine.copernicus.eu/services-_portfolio/access-_to-_product together with the new Mean Dynamic Topography called MDT_CNES-CLS18 available at https://www.aviso.altimetry.fr/en/data/products/auxiliary-_products/mdt.html. The new MDT is derived from the CNES-CLS15 MSS, the GOCO05S geoid model together with the latest versions of altimetric (for the period 1993–2012) and in situ data. The spatial resolution is 1/8. As the SLA is available at 1/4°, we linearly interpolated the SLA to 1/8° in order to calculate the current under the geostrophic approximation.

$$u_{geo} = -\frac{g}{f} \frac{\delta(SLA + MDT)}{\delta y}, \text{ and } v_{geo} = \frac{g}{f} \frac{\delta(SLA + MDT)}{\delta x} \quad (12)$$

For the Along-Track estimates and due to the fact that the Agulhas current has a strong SSH-gradient signature, we also inferred the geostrophic current perpendicular to the orbital tracks of the altimeter Jason-2. The Along-Track altimetry data set was obtained from the AVISO Geophysical Data Records (GDR) available at <https://www.aviso.altimetry.fr>. We used the 1 Hz (5.8 km) Jason-2 SSH corresponding to tracks #20 and #96 and derived geostrophic velocities from the Along-Track ADT obtained by subtracting the mean sea surface height and adding the mean dynamic topography. This methodology is basically the same as that used by Krug and Tournadre (2012).

3.1.2. Synthetic Aperture Radar-Derived Surface Current Field and Sentinel-1 SAR Roughness

Although the geostrophic current estimates are derived from the sea level height which results from an integration over the water column, they only represent an estimate of the geostrophic current and do not represent the total surface current. In order to compare with an estimate of the total surface current we used the radial velocity map estimated from the Advanced Synthetic Aperture Radar (ASAR) measurements on the ENVISAT satellite mission (2002–2012) (Chapron et al., 2005; Johannessen et al., 2008; Rouault et al., 2010) available at <https://cersat.ifremer.fr>. The basic principle involves using the Doppler centroid information in the radar signal to extract the ocean surface velocity. In the Agulhas region, for example, Johannessen et al. (2014), quantitative estimation of the current's speed can be reliably calculated along the radar line-of-sight which coincides closely with the main current direction 15° from the north (anti-clockwise). For ASAR measurements, the resulting average map at 1/8° resolution builds on 329 ascending acquisitions, accumulated during the 2007–2011 period. As the time period for the ASAR measurements does not overlap with the time period for the present study, we compared only the average ocean surface velocity over each time period.

To characterize our spatially and temporally co-located results, we used the SAR imagery and one image in particular from the Sentinel-1 mission taken on December 5, 2016, thus coinciding with our study period. Oceanic fronts are often revealed by high resolution products such as sea surface temperature or ocean color but also by sea surface roughness. The sea surface current gradients generally impact the roughness of the ocean and provide a means to study the sharp oceanic front (Kudryavtsev et al., 2012; Raschle et al., 2020). The nominal resolution is about 20 m and data are available at <https://scihub.copernicus.eu/>.

3.1.3. Sea Surface Temperature and Ocean Color

The sea surface temperature (SST) and ocean color (Chlorophyll-A) data used here were derived from Aqua and Terra MODIS sensors with a resolution of approximately 1 km at nadir. We used Level-2 (L2) data which represents the measurements at full swath resolution. Both SST and ocean color data were obtained from the NASA Ocean Biology Processing Group (OBPG).

3.2. In Situ Data

3.2.1. ACT Experiment

To further test the retrieved estimates, we also considered surface velocities from the Agulhas Current Time-series (ACT) experiment. We use the gridded cross-sectional velocities based on in situ current meter measurements (Beal et al., 2015). Data can be downloaded at <https://beal-agulhas.rsmas.miami.edu/data-and-products/index.html>. Moorings, located beneath the altimeter Jason-2, track 96, all include ADCP instruments oriented toward the surface enabling the estimation of the near-surface current. Vessels generally have a draft inferior to 20 m. From the ACT products, we then used the mean cross-sectional velocity over the 3-year experimental period at two different depths: 0 and 20 m. Small differences were found, indicating a weak vertical shear. To compare the current estimates obtained from the different sensors, we systematically rotated the zonal and meridional velocity components by 64° to coincide with the cross-track velocity directions of both the ACT experiment and Jason-2, track #96. The ACT array deployment and the Jason-2, track #96 were oriented 15° clockwise from the perpendicular of the continental slope in order to align with the core direction of the main path of the Agulhas current. The cross-track velocities of both the ACT and Jason-2 track #96 were thus very close to the total velocity of the current.

3.2.2. Drifting-Buoys

When possible, comparisons with Lagrangian estimates from drifting-buoys were also considered. Data from a total of 15 drifting-buoys, passing through the region of interest in 2016, were available at <http://www.aoml.noaa.gov/envids/gld/> (Lumpkin et al., 2013). Lagrangian drifters are surface floats equipped with a holey-sock drogue centered at 15 m.

4. Results and Discussion

4.1. Annual Average

Time averages are of interest for several reasons. First, the geostrophic current estimates are obtained from Equation 12 which contain the MDT and the SLA. Although the MDT corresponds to an average over a number of years (1992–2013), the annual average of SLA (for 2016) in the Agulhas region is close to zero. This means that comparisons can be drawn between the mean geostrophic current calculated for different periods and other sources of oceanic current estimates such as the ASAR or the AIS-derived current. Second, the time average does not suffer from bias and smoothing linked to interpolation techniques.

4.1.1. ASAR and MDT

Data from the ASAR corresponds to a radial velocity in a direction oriented 15° clockwise from the zonal component. When both components of the current are available, we applied a rotation to conform to the radial direction of the ASAR and then compared the result with the appropriate rotated component. Results are presented in Figure 8. Plot (a) illustrates the time average of the ASAR radial velocity estimates obtained from the 329 ascendant paths during the 2007–2011 period. The current's core is clearly distinguishable and the maximum current in the radial line of sight is observed between 26°E and 28.5°E . The current reaches up to $\approx 1.7\text{ ms}^{-1}$ in this area. Plot (b) shows that the magnitude of the mean geostrophic current calculated for the same period (2007–2011), in the same radial line of sight and corresponding to the last available MDT (2018), is similar to the ASAR radial velocity estimates. The maximum current is, however, located more westward, that is, between 25°E and 27°E . Regarding the estimates of the ocean surface current represented in plot (c) for the first guess and (d) for the second guess, we note a more faithful similarity with the ASAR estimates confirmed in plot (e) where we calculated the difference between the radial velocities

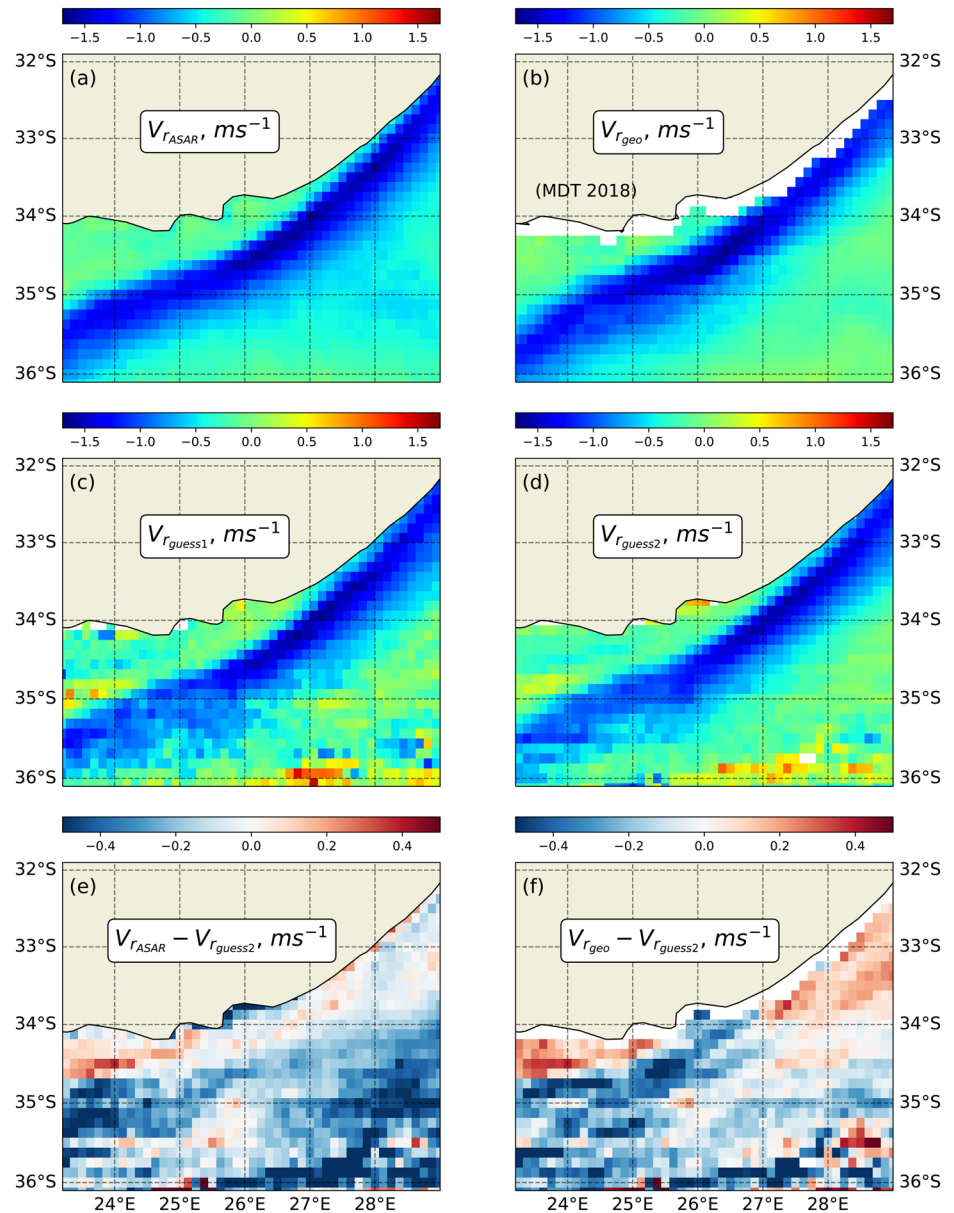


Figure 8. Time average maps of radial surface velocity from: (a) ASAR based range-Doppler velocity from 2007 to 2011. (b) Surface geostrophic current derived from the 2007–2011 period (2018 MDT). (c) First guess of the oceanic surface current. (d) Second guess of the oceanic surface current. The velocities in (b–d) are rotated by 15° to conform with the ASAR radial range velocities. All maps have a spatial grid resolution of $1/8^\circ$. (e) Difference between the ASAR radial velocities and the AIS radial velocities. (f) Difference between the mean geostrophic radial velocities (2007–2011) and the mean AIS radial velocities. The color bar indicates surface speed in ms^{-1} .

obtained from the ASAR and the AIS. Nevertheless, it seems that the current estimates from the AIS are weaker in the south-western area. Regarding the difference between the mean radial velocity of the geostrophic current and the AIS-derived current, we note a positive difference in the north-eastern part, which means that the geostrophic current is underestimated near the coast. Additionally, we note no such difference in plot (e) around longitude 25.5°E and latitude 34.5°S . In this case, the geostrophic current seems too large and too close to the coast compared to the ASAR and AIS-derived estimates. It may be noted that the difference between the first and second guesses clearly highlights a difference in noise level.

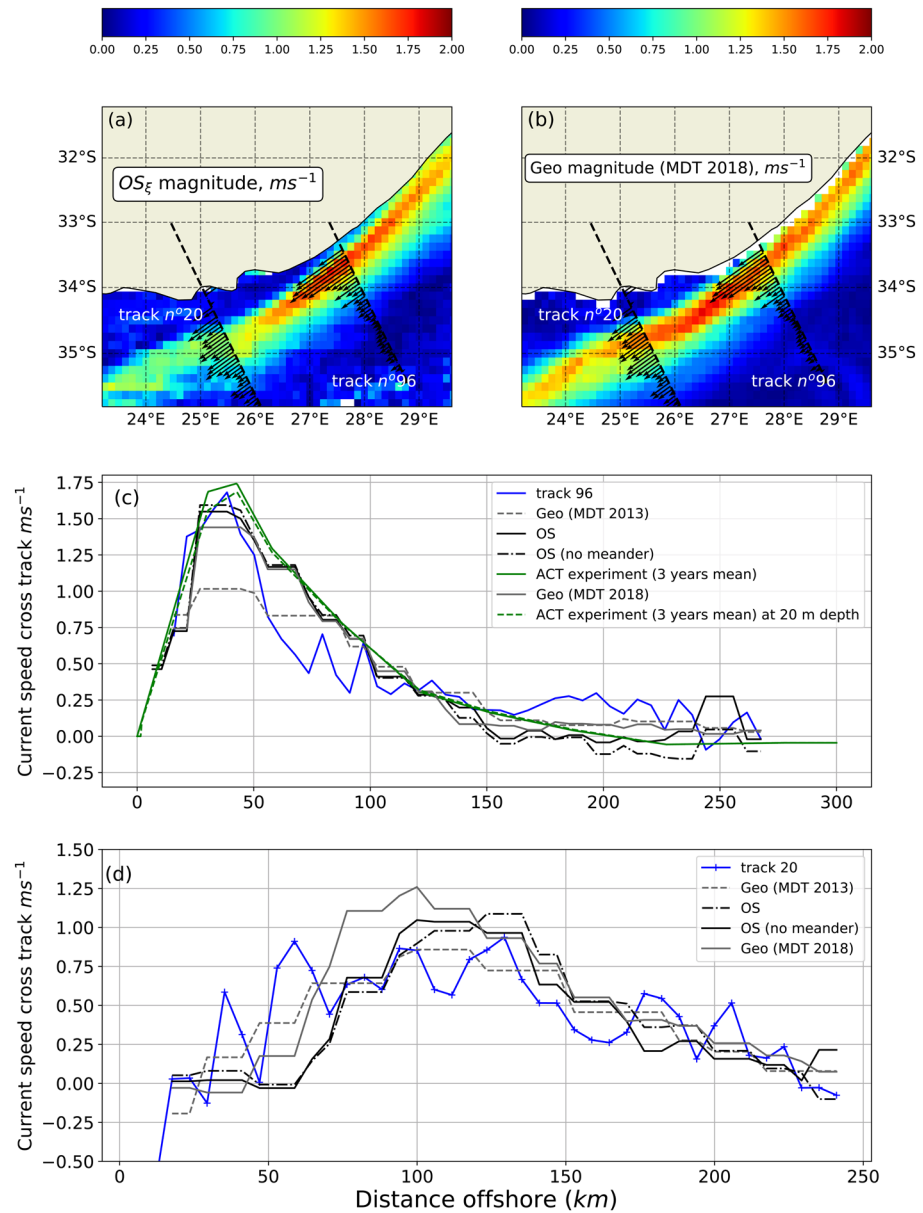


Figure 9. (a) Time average of the magnitude of our ocean surface current estimates. (b) Time average of the magnitude of the oceanic current derived from the 2018 MDT. Quivers represent the time average for the Along-Track geostrophic velocities for the Jason-2 tracks 20 and 96. (c) In blue, the cross-track velocity from Jason-2 track 96 for the year 2016 (mean of 20 altimeter geostrophic velocities). In green, the cross-track surface velocities from the gridded data set of the ACT experiment averaged over 3 years for the surface (full line) and at 20 m depth (dashed line). The oceanic surface current velocity is represented by a black full line for the year 2016 and current velocities associated to the two MDT estimates are shown in gray (full line for 2018, dashed line for 2013). (d) Same as (c) but for the altimeter Jason 2 track 20.

4.1.2. ACT, MDT, and Along-Track Altimetry

The area covered in this study has been intersected by both the Jason-2 altimeter tracks 96 and 20, and the corresponding in situ ACT deployment. Comparisons are reported between the reconstructed AIS surface current, the Along-Track geostrophic velocities derived from the Along-track SLA and MDT, and those estimated from the two-gridded MDT data (2018 and 2013). As the time periods do not overlap, only the mean gridded cross-track surface current velocities from the ACT experiment (2010–2013) are considered (Beal

et al., 2015). Figure 9 shows maps of the surface current magnitudes for (a) the oceanic surface current from the AIS messages and (b) the mean geostrophic current obtained from the 2018 MDT. Obtained as described in the previous paragraph, the current's core is shown very close to the coast and seems strongly steered by the continental slope. Estimates from the new MDT are slightly weaker than the estimates of the oceanic surface current derived from AIS messages. We note the opposite effect in the south-western part where the current flows farther from the coast. These observations are quantified in Figure 9 where we compare (c) the along cross-track velocity for the Jason-2 track 96 associated with the ACT time series experiment and (d) the along cross-track velocity for the Jason-2 track 20. On both graphs, although the previous Mean Dynamic Topography (2013 MDT, dashed gray line) was clearly much weaker than all others estimates, the more recent Mean Dynamic Topography (2018 MDT, full gray line) is much closer to both the ACT experiment and the mean cross-track velocity from track 96 (blue line) but seems rather high in comparison to track 20. It is interesting to note that both the geostrophic velocities and the AIS reconstructed velocities are close to the ACT measurements, though both slightly weaker.

4.1.3. Kinematics Properties

Among the key variables in ocean dynamics are vorticity and divergence. Obviously these quantities are linked to the divergent-free flow field OS_r and the divergence to the rotational-free flow field OS_d . For example, in the Quasi-Geostrophic model, the derivative of the surface vorticity is modified by the surface divergence when the fluid is considered incompressible. Moreover, the oceanic surface divergence is often associated to the oceanic front and can be easily detected from sea surface temperature, ocean color and SAR imagery. In Figures 10a and 10b the average annual SST from the MODIS Aqua Sensor is presented together with the average annual Chlorophyll-a concentration for the year 2016. The region is clearly divided between the warm, poor (in terms of Chlorophyll-a) and the cold, rich waters. From the average annual OS_r current, in these regions we can attribute positive and negative vorticity to the warm, poor waters and the cold, rich waters respectively (Figure 10c). The same can be seen with the divergence calculation presented in Figure 10d. Here, the cold, rich waters correspond to positive divergence (up-welling), whereas the warm, poor waters correspond to negative divergence (down-welling). It is important to note that the Chlorophyll-a concentration is in log-scale and the level corresponding to the value -1 is plotted in Figure 10b. This line approximately corresponds to the level of zero divergence in Figure 10d. In Figures 10e and 10f the average annual magnitude of the divergent-free (OS_r) and rotational-free (OS_d) flows are shown. The first field shares the same mathematical property of being a divergent-free field as the velocity field derived from the MDT (Figures 8b and 9b). When compared, we notice a similar value $\approx 1.5 \text{ ms}^{-1}$ in the north-eastern part but a notable difference arises in the south-western part where the current derived from the MDT is stronger. Interestingly, this part corresponds to the highest magnitudes of the average annual rotational-free (OS_d) field. Indeed, this magnitude can be as high as 25 cms^{-1} and is essentially oriented southwards. Therefore, we suggest that the meridional component of the total current estimates (OS_t) will have a more significant part of rotational-free flow (OS_d) than will the zonal component. Moreover, the oceanic current estimates derived from the altimetry are better solved in the zonal direction than in the meridional one. Most often, this is due to the north-south orientation of the nadir-looking altimeter ground tracks, allowing more accurate zonal surface currents to be derived via the geostrophic approximation. Nevertheless, this approximation does not take into account the ageostrophic processes present in the total estimates of the current (OS_t) represented in our study by the rotational-free flow. For this particular region, this may be another source of error relating to the meridional component of the geostrophic current.

4.2. Space-Time Co-location Synergy and Validations

In this part we analyze and compare three different situations at three different times before testing our estimates with the spatially and temporally co-located velocity estimates from the drifting-buoys.

4.2.1. Sentinel-1 SAR Roughness

Contrary to the average annual current which strictly follows the continental shelf, the Agulhas current is sometimes disrupted by cyclonic events, also known as meanders or natal pulses (Beal & Elipot, 2016; Lutjeharms et al., 1989). These events occur around 1.6 year^{-1} (Rouault & Penven, 2011). A propagating natal pulse can be clearly observed on the SAR image obtained from the Sentinel-1 mission on December

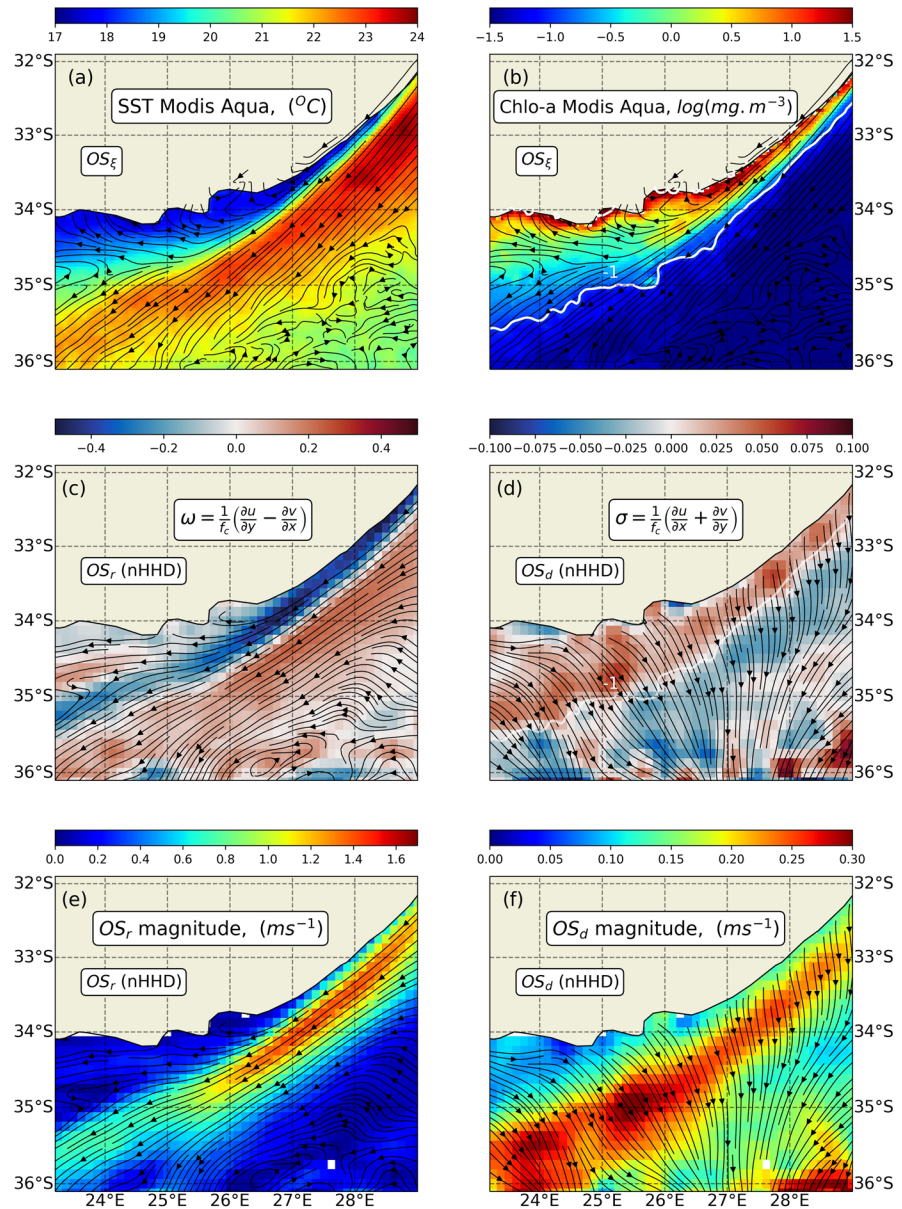
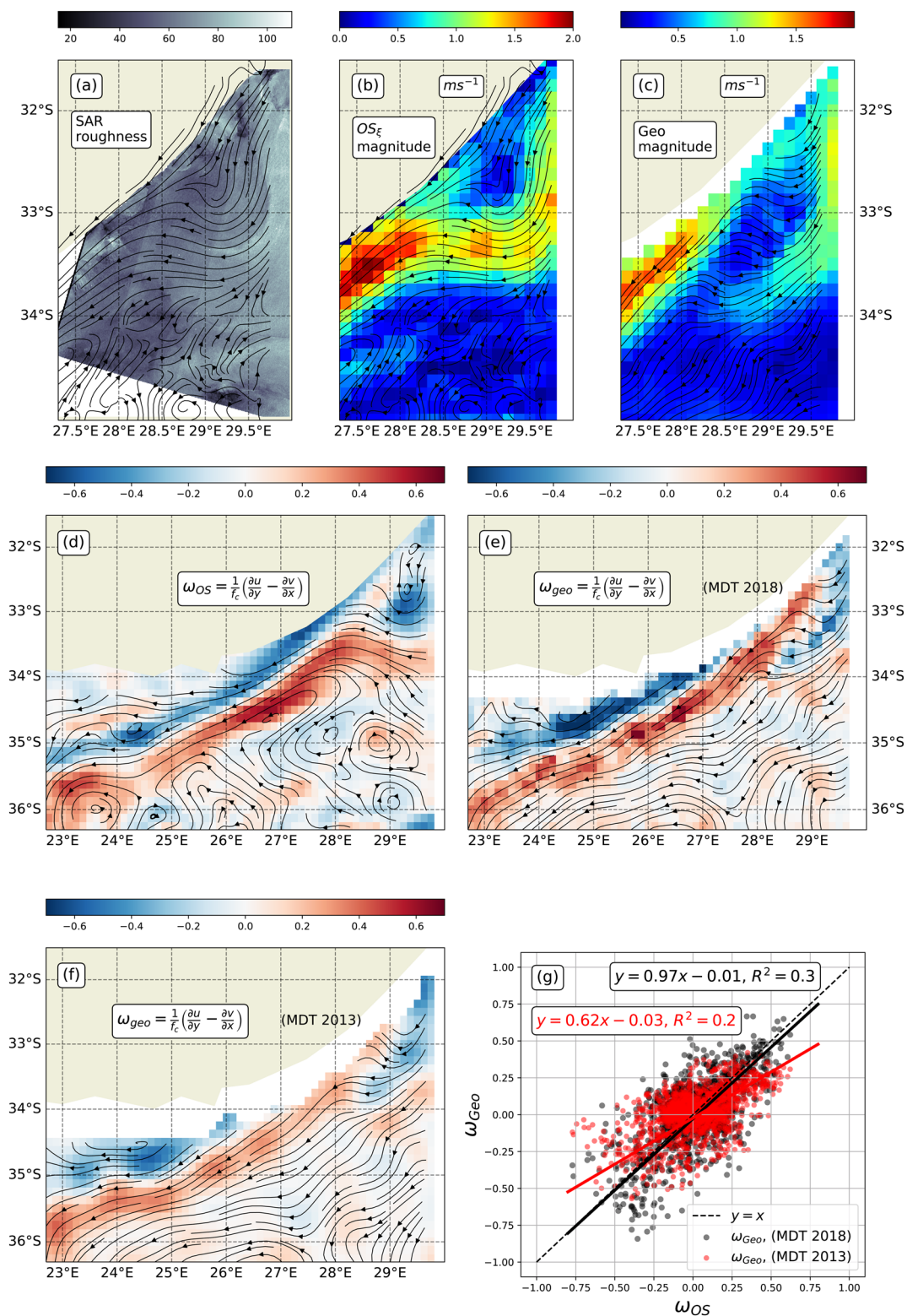


Figure 10. All maps correspond to annual mean (2016). (a) SST MODIS with the streamlines of the total oceanic surface current field. (b) Chlorophyll-a also with the streamlines of the total oceanic surface current field. (c) Vorticity with the divergent-free flow field (OS_r). (d) Divergence with the streamlines of the rotational-free flow field (OS_d). (e and f) represent the magnitude of the divergent-free flow field and the rotational-free flow field associated with their own streamlines.

5, 2016, presented in Figure 11a. To compare the OS and geostrophic gridded current estimates, their magnitudes with associated streamlines are shown in Figures 11b and 11c respectively. We clearly note that the streamlines associated to the OS_ξ current follow the shape of the meander present in the SAR Roughness image more closely than do the streamlines issued from the geostrophic gridded current. In this specific case, it may be argued that this is caused by the fast evolving shape of the meander in contrast to the time resolution of the altimeter-derived geostrophic current estimates. Figure 11 shows snapshots, for the same day, of the vorticities (normalized by the Coriolis frequency) from (d) the divergent-free OS_r current, (e) the geostrophic current with the 2018 MDT and (f) the geostrophic current with the 2013 MDT. The vorticities from the OS_r current and the geostrophic current with the 2018 MDT are rather close in terms of magnitude,



an observation easily seen in the scatter plot in Figure 11g. The slope of the regression between the two vorticities is close to one (0.97), although the R-squared value is rather weak (0.3). Regarding the vorticity of the geostrophic current with the 2013 MDT, shown in plots (f) and (g), we immediately note the difference. Indeed the vorticity is much weaker, as confirmed in scatter plot (g) (red dot) with the corresponding regression slope no longer close to one, but equal to 0.62 with a R-squared value of 0.2. This result illustrates the net improvement of the last MDT on the previous one. However, some cyclonic and anti-cyclonic structures are clearly present in the vorticity derived from the OS_r current, shown in Figure 11d, while absent in the altimetry-derived vorticities shown in Figures 11e and 11f.

4.2.2. SST and Ocean Color

Here we illustrate two situations of interest where the MODIS Terra sensors captured the SST signature and ocean color. The first occurred during a meander event on April 11, 2016. As previously shown in Figure 11, a propagating natal pulse is clearly expressed on the SST field. In this case, however, the meander was located in the south-western part of the region (Figure 12a). The total oceanic surface OS_r streamlines obtained, closely follow the SST iso-lines and thus the meander. Such circulation is likely to cause vertical velocity and induce up-welling (Goschen et al., 2015; Leber et al., 2017). Indeed, these authors' findings demonstrate that two mechanisms are responsible for induced up-welling events: the presence of a meander and northeasterly winds. As an illustration of the up-welling sites, Figure 12b shows the concentration of chlorophyll-a. The streamlines associated to the divergent component (OS_d) of the velocity field clearly originate in the highest chlorophyll-a concentration areas as is the case for the maps showing annual average illustrated in Figures 10d and 10f. The areas of highest concentration are always located near the shore, on the continental shelf. During a meander event, however, higher concentrations are present over a larger geographical area. As previously, the line corresponding to the value -1 in the log scale of the chlorophyll-a concentration is reported on the map in Figure 12c. As was the case for the annual average, we clearly observe that the line separating the areas of high and poor chlorophyll-a concentration coincides quite well with the areas of positive and negative divergence.

The second situation of interest occurred on May 18, 2016. This period was meander-free but showed the presence of northeasterly winds. Results are shown in Figures 12d–12f. In this situation, the SST gradient is more pronounced between the current's core and the continental shelf which concentrates the highest levels of Chlorophyll-a. The area is smaller than in the first situation (meander). Roughly the same observations can be made regarding the separation between rich and poor regions (in terms of Chlorophyll-a) and the correspondence with the positive and negative divergence. An interesting phenomenon can be observed in the south-western area where a thin filament of Chlorophyll-a follows the Agulhas current along its inner side. This thin filament clearly corresponds to an area of high positive divergence (Figures 12e and 12f).

4.2.3. Drifting-Buoys

For the year 2016, we could select 15 drifting-buoys within our study site from the AOML catalog. Their trajectories are presented in the subplot of Figure 13a. Figures 13a and 13b show maps corresponding to the oceanic current estimates OS_r and geostrophic estimates (Geo) during a meander event in the beginning of March. A week before the date represented on these maps, on February 24th, a drifting-buoy entered the area in the north-eastern part and drifted northwards before interacting with the main current and being advected south-west following the current caused by the meander. Although the correlation and Root Mean Square Error (RMSE) between the OS_r or Geo velocities and the velocities issued from this drifter in particular are close, some differences do exist between the two maps. First, near the coast and between the longitudes 27°E and 28° the south-westward current is much stronger when considering the OS_r estimates.

Figure 11. All the maps correspond to December 5, 2016. (a) SAR Roughness, streamlines correspond to the oceanic surface current (OS_r). (b) Magnitude and associated streamlines of the oceanic surface current (OS_r). (c) Magnitude and associated streamlines of the altimetry-derived geostrophic gridded current (Geo). (d) Vorticity, obtained from the OS_r current with the associated streamlines. (e) Vorticity of the altimetry-derived geostrophic gridded current with the 2018 MDT with the associated streamlines. (f) Vorticity of the altimetry-derived geostrophic gridded current with the 2013 MDT with the associated streamlines. (g) Scatter plot showing the vorticity from the OS_r current and the vorticity from the altimetry-derived geostrophic gridded current with the 2018 MDT (black dot) and the 2013 MDT (red dots).

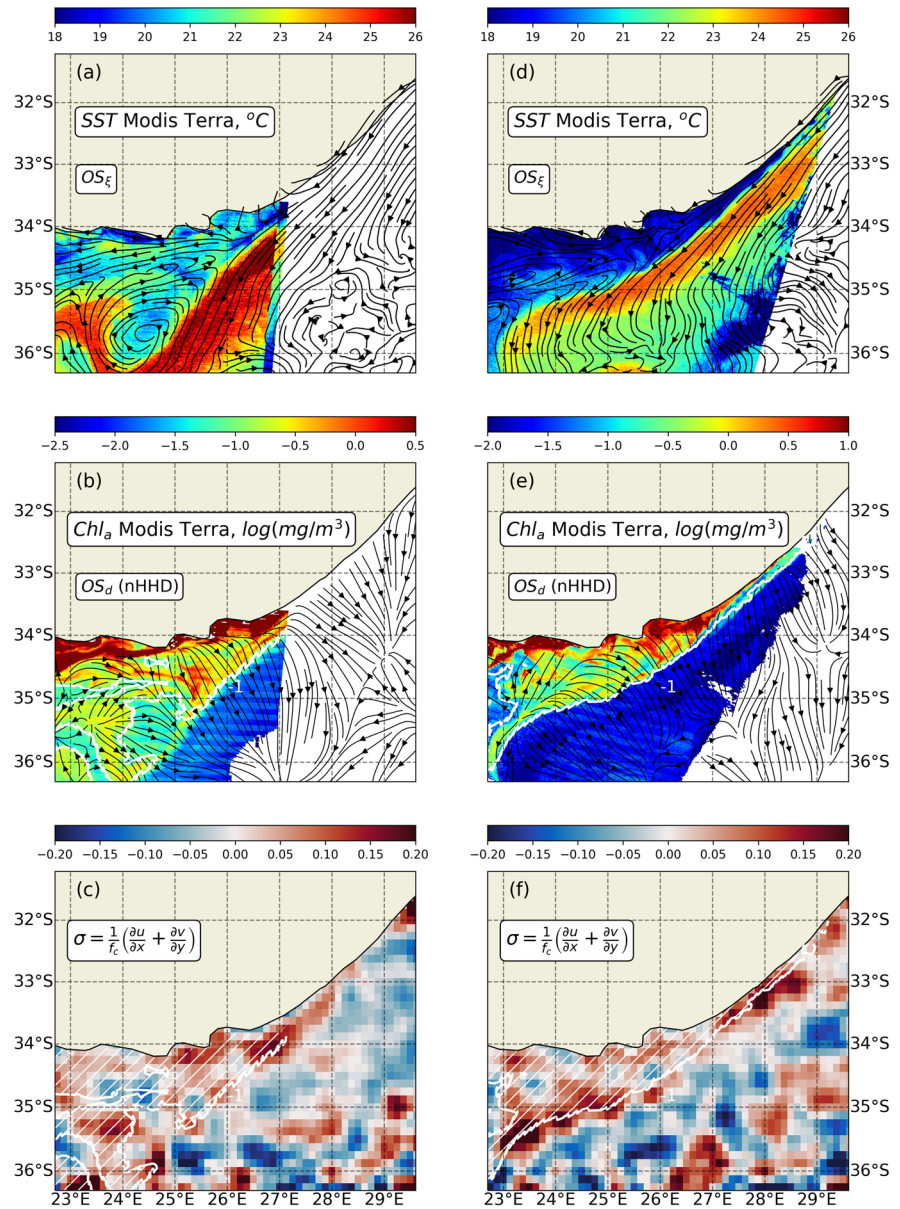


Figure 12. (a) Sea surface temperature in degrees Celsius obtained from the MODIS Terra sensor for April 11, 2016. Streamline represents the total AIS current estimates. (b) Ocean color (Chlorophyll-a) in a logarithmic scale obtained from the MODIS Terra sensor, same day as (a). Streamline represents the divergence component of the current. (c) Same as (a) but on May 18, 2016. (d) Same as (b) but on May 18, 2016.

The same phenomenon exists if we consider the divergent-free flow field (OS_r) instead. Second, the south geographical extension of the meander is larger with the OS_r estimates.

To study the difference between the two products and considering the velocities of the drifters as a ground truth, we systematically co-located (in both time and space) the velocities associated to the drifting-buoys with our estimates and those from the Geo. Figure 11c shows the comparison between the total zonal surface current (U_z) (in blue) and the divergent-free (U_r) (in red) with the zonal velocities of the drifting-buoys. We note a better correlation ($r = 0.83$ vs. $r = 0.76$) and lower RMSE (0.32 vs. 0.38) when considering the zonal divergent-free component (U_r) with the zonal velocities of the drifting-buoys. It is important to note that Figure 10f shows the annual average of the rotational-free flow field and though weaker than the meridional component, a positive zonal component appears. It seems logical that the total zonal current

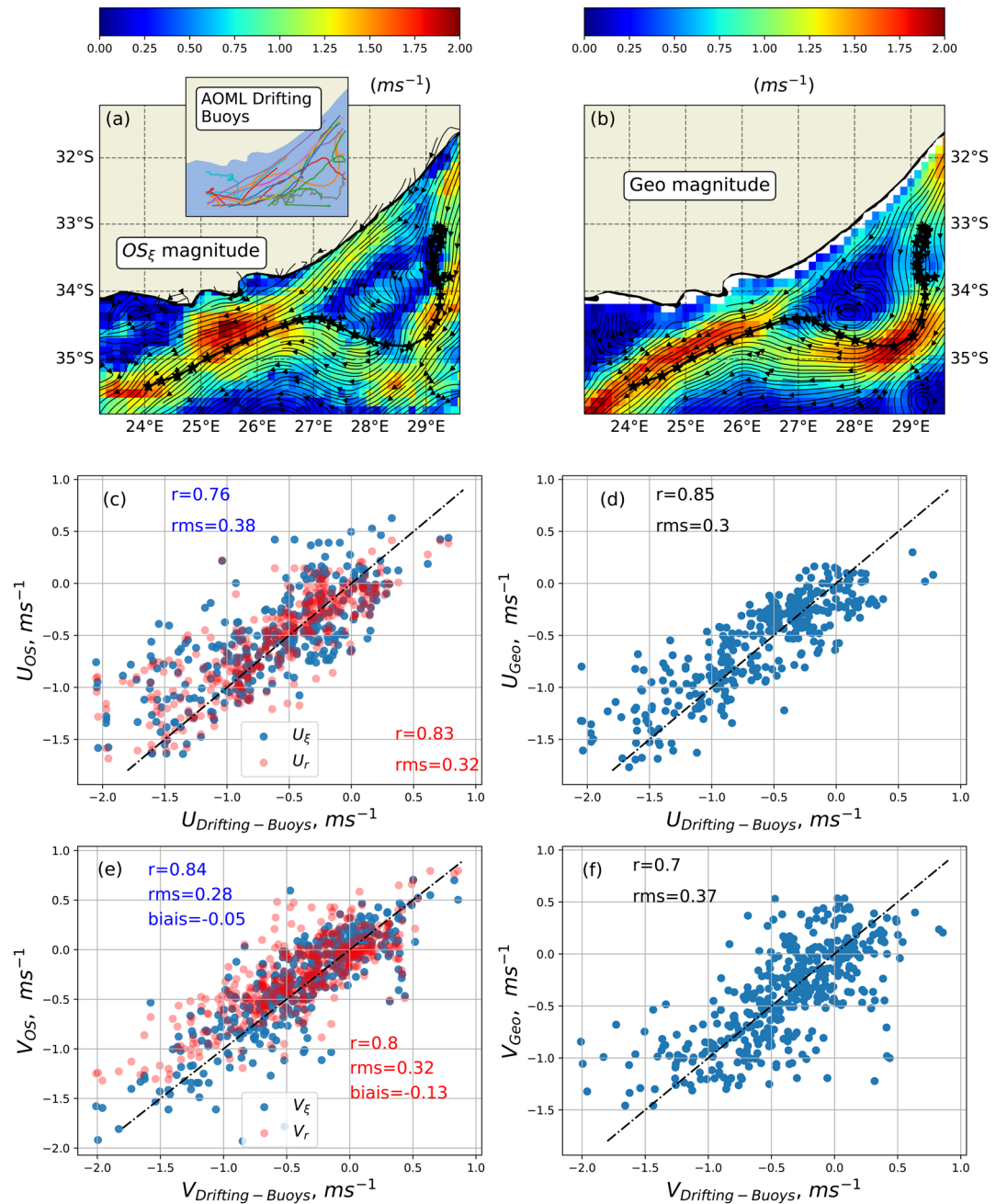


Figure 13. (a) Ocean Surface current magnitude for March 1, 2016. The black dotted line shows an example trajectory of one of the drifting-buoys between February 24th and March 6th. The trajectories of the 15 drifting-buoys considered in this study are represented in the sub-graph. (b) Same as (a) but for the geostrophic estimates (Geo) of the current. (c) Scatter plot of the zonal component of the total velocity field versus the zonal velocity of the drifting-buoys (in blue). In red, the zonal component of the total velocity field is substituted by the zonal curl component. (d) Scatter plot of the zonal component of the geostrophic velocity field versus the velocity of the drifting-buoys. (e) Scatter plot of the meridional component of the total velocity field versus the meridional velocity of the drifting-buoys (in blue). In red, the meridional component of the total velocity field is substituted by the meridional curl component. (f) Scatter plot of the meridional component of the geostrophic velocity field versus the meridional velocity of the drifting-buoys.

estimates U_{ξ} are weaker (in absolute value) than the divergent-free zonal estimates U_r . This is somewhat what is observed when looking at Figure 13c. Moreover, the scatter plot shown in Figure 13d comparing the zonal Geo estimates to the zonal velocities of the drifting-buoys is very similar to that obtained with the divergent-free flow field ($r = 0.85$, $\text{rmse} = 0.3$). The drifting-buoy drogues are at 15 m depth which is very similar to the draft of vessels. Why the divergent-free component U_r is closer to the zonal velocity of the drifting-buoys remains unanswered. One explanation may come from the errors which are larger in the zonal direction than in the meridional one, as demonstrated in the optimal interpolation Section 2.5

When we compare the meridional velocities V_{ξ} and V_r to the meridional velocity of the drifting-buoys we find quite the opposite result, which is definitively far easier to interpret. Indeed, the analysis of the scatter plot in Figure 13e shows a stronger correlation with the total V_{ξ} in blue ($r = 0.84$, $\text{rmse} = 0.28$) than with the divergent-free V_r in red ($r = 0.8$, $\text{rmse} = 0.32$). Moreover, a clear bias is observed when comparing the total meridional component with the meridional divergent-free component (≈ -0.05 for the total current vs. ≈ -0.13 for the divergent-free current). This indicates that the meridional divergent-free component underestimates the real current represented by the drifting-buoys. The same can be observed with the meridional Geo velocities where the lowest absolute values never exceed -1.5 ms^{-1} as is the case for the meridional divergent-free current V_r . This, however, is clearly not the case for the total estimates V_{ξ} , the absolute values of which quite regularly exceed -1.5 ms^{-1} . In terms of the annual average, Figure 10f shows magnitude values around 25 cm.s^{-1} oriented almost southward for the rotational-free current. This is in line with the bias found between the meridional velocity of the divergent-free current and the meridional velocity of the drifting-buoys. Given that the drifting-buoys' drogues are at a depth of 15 m and that the draft of vessels is of the same order but integrated from the surface to the draft, we guess that our current estimates correspond to a depth inferior to 15 m. This could be the reason for the difference observed between the bias of 0.13 cm.s^{-1} and the magnitude of the rotational-free current of $\approx 0.25 \text{ cm.s}^{-1}$. Another possible explanation could be the spatio-temporal sparsity of the drifting-buoys. For this part, however, it seems reasonable to conclude that the extremes values in the meridional velocity of the drifting-buoys are out of the geostrophic equilibrium.

5. Conclusion

In this study, we have demonstrated that improved estimations of upper ocean surface velocities can be obtained over the core region of the Agulhas Current, when using selected AIS messages. This demonstration relies largely on the intense maritime traffic off the South African coast. In the present study, a wealth of information is combined with all available *a priori* surface current estimates (particularly those derived from satellite altimetry and drifting-buoys) in order to develop an improved spatio-temporal surface current monitoring system. Similar strategies may then also be applied to other regions characterized by intense maritime traffic and will be subject for future investigations, for example, the Mediterranean sea with intense traffic between the Strait of Gibraltar and the Suez canal, also northern and eastern regions of the Arabian Sea and in proximity to large river mouths.

The AIS data does not directly provide vessel speeds with respect to the moving ocean (i.e., speed through water). To overcome this lack of information and in order to directly derive the upper ocean current, the interpretation framework can be built on a homogeneity assumption: that is, all vessels, chosen within a given space-time interval, encounter the same sea surface conditions. In the Agulhas region of interest, this space-time interval can be adjusted according to the density of maritime traffic. A second guess reduces the space-time resolution to one day and $1/8^\circ$. During transient events the differences between our estimates and standard altimeter geostrophic current estimates are notable. These transient events may move relatively fast and not be sufficiently sampled by altimeter measurements.

Further comparisons performed using data from in situ drifting-buoys, ADCP measurements (ACT experiment), as well as average Doppler-derived surface current from satellite SAR measurements, all reveal a general (anticipated) underestimation of the surface current estimates obtained by interpolated altimeter products. To recall, noise in the classic along-track altimeter observations and the distance between ground tracks are strong limiting factors when deriving a 2D Sea-surface height (SSH) field to scales smaller than 100 km at mid-latitudes (Chelton et al., 2019). The future SWOT SAR-interferometry wide-swath altimeter mission is designed to largely improve present-day capabilities, resolving spatial scales down to 15–30 km,

with unique instantaneous 2D SSH snapshots (Morrow et al., 2019). Combining AIS-derived space-time surface currents and these future measurements may provide unique opportunities to better assess highly variable upper ocean dynamics.

Furthermore, in view of the existing need for a more comprehensive monitoring system for the Agulhas Current, these results are encouraging to consider the ever-increasing availability of AIS messages for routine quantitative monitoring of surface current conditions, and to better evaluate the leakage of warm, saline waters from the Indian Ocean into the Atlantic Ocean (Beal et al., 2011; de Ruijter et al., 1999). Combining surface information with in situ information can directly serve to more accurately represent Agulhas ring transport and exchanges (Nencioli et al., 2018). Modeling surface current interactions in standard wave numerical models is also an active area of research (Ardhuin et al., 2017). In the Agulhas current region, strong currents cause significant swell ray deflection and localized trapping phenomena (e.g., Quilfen & Chapron, 2018; Quilfen et al., 2018). A direct benefit of the increased availability and accuracy of combined satellite observations, including imaging (Kudryavtsev et al., 2017a, 2017b) and AIS messages would be a significant improvement in navigation safety in the region.

Data Availability Statement

The raw AIS data were obtained from ORBCOMM. Underlying raw AIS data (i.e., individual vessel tracks) are publicly available from source data providers and may or may not require a fee to be accessed, depending on user affiliation and terms of use. The SST and mean Doppler-derived surface current (SAR) products are available at <http://cersat.ifremer.fr/>. The data from the drifting-buoys is available at <http://www.aoml.noaa.gov/envids/gld/>. The gridded reprocessed absolute geostrophic velocities from AVISO, distributed by CMEMS are available at <http://marine.copernicus.eu/services-portfolio/access-to-products/>. The data from the JASON-2 altimeter tracks 96 and 20 are available at <https://www.aviso.altimetry.fr>. Regarding the ACT experiment, the data can be downloaded at <https://beal-agulhas.rsmas.miami.edu/data-and-products/index.html>.

Acknowledgments

We thank two anonymous reviewers for their critical review of our work contributing to the improvement of the manuscript. We also thank the GlobCurrent project (<http://www.globcurrent.org>) as this work was partly supported by the European Space Agency through ESA-ESRIN DUE GlobCurrent Project, Contract No. 4000109513/13/I-LG.

References

- Ardhuin, F., Gille, S. T., Menemenlis, D., Rocha, C. B., Raschle, N., Chapron, B., et al. (2017). Small-scale open ocean currents have large effects on wind wave heights. *Journal of Geophysical Research: Oceans*, 122(6), 4500–4517. <https://doi.org/10.1002/2016JC012413>
- Beal, L. M., De Ruijter, W. P. M., Biastoch, A., Zahn, R., & S. W. G. (2011). On the role of the Agulhas system in ocean circulation and climate. *Nature*, 472, 429.
- Beal, L. M., & Donohue, K. A. (2013). The great whirl: Observations of its seasonal development and interannual variability. *Journal of Geophysical Research: Oceans*, 118(1), 1–13. <https://doi.org/10.1029/2012JC008198>
- Beal, L. M., & Elipot, S. (2016). Broadening not strengthening of the Agulhas current since the early 1990s. *Nature*, 540, 570–573. <https://doi.org/10.1038/nature19853>
- Beal, L. M., Elipot, S., Houk, A., & Leber, G. M. (2015). Capturing the transport variability of a western boundary jet: Results from the Agulhas current time-series experiment (act). *Journal of Physical Oceanography*, 45(5), 1302–1324. <https://doi.org/10.1175/jpo-d-14-0119.1>
- Bhatia, H., Pascucci, V., & Bremer, P.-T. (2014). The natural Helmholtz-Hodge decomposition for open-boundary flow analysis. *IEEE Transactions on Visualization and Computer Graphics*, 20(11), 1566–1578. <https://doi.org/10.1109/tvcg.2014.2312012>
- Bretherton, F. P., Davis, R. E., & Fandry, C. B. (1976). A technique for objective analysis and design of oceanographic experiments applied to mode-73. *Deep Sea Research and Oceanographic Abstracts*, 23, 559–582. [https://doi.org/10.1016/0011-7471\(76\)90001-2](https://doi.org/10.1016/0011-7471(76)90001-2)
- Bryden, H. L., Beal, L. M., & Duncan, L. M. (2005). Structure and transport of the Agulhas current and its temporal variability. *Journal of Oceanography*, 61(3), 479–492. <https://doi.org/10.1007/s10872-005-0057-8>
- Caesar, L., McCarthy, G. D., Thornalley, D. J. R., Cahill, N., & Rahmstorf, S. (2021). Current atlantic meridional overturning circulation weakest in last millennium. *Nature Geoscience*, 14(3), 118–120. <https://doi.org/10.1038/s41561-021-00699-z>
- Chapron, B., Collard, F., & Ardhuin, F. (2005). Direct measurements of ocean surface velocity from space: Interpretation and validation. *Journal of Geophysical Research*, 110(C7), c07008. <https://doi.org/10.1029/2004JC002809>
- Chelton, D. B., Schlax, M. G., Samelson, R. M., Farrar, J. T., Molemaker, M. J., McWilliams, J. C., & Gula, J. (2019). Prospects for future satellite estimation of small-scale variability of ocean surface velocity and vorticity. *Progress in Oceanography*, 173, 256–350. <https://doi.org/10.1016/j.pocean.2018.10.012>
- de Ruijter, W. P. M., Biastoch, A., Drijfhout, S. S., Lutjeharms, J. R. E., Matano, R. P., Pichevin, T., et al. (1999). Indian-Atlantic interocean exchange: Dynamics, estimation and impact. *Journal of Geophysical Research*, 104(C9), 20885–20910. <https://doi.org/10.1029/1998JC900099>
- Goschen, W. S., Bornman, T. G., Deyzel, S. H. P., and Schumann, E. H. (2015). Coastal upwelling on the far eastern Agulhas bank associated with large meanders in the Agulhas current. *Continental Shelf Research*, 101, 34–46. <https://doi.org/10.1016/j.csr.2015.04.004>
- Guichoux, Y. (2015). Sea surface currents calculation using vessel tracking data. In *Ocean dynamics 2.0 poster, EURASC symposium*.
- Guichoux, Y., Lennon, M., & Bouvier, N. (2016). Sea surface currents calculation using vessel tracking data. *Maritime Knowledge Discovery and Anomaly Detection Workshop*. <https://doi.org/10.2788/025881>

- Huang, N. E., Shen, Z., Long, S. R., Wu, M. C., Shih, H. H., Zheng, Q., et al. (1998). The empirical mode decomposition and the Hilbert spectrum for nonlinear and non-stationary time series analysis. *Proceedings of the Royal Society of London. Series A: Mathematical, Physical and Engineering Sciences*, 454, 903–995. <https://doi.org/10.1098/rspa.1998.0193>
- Inazu, D., Ikeya, T., Waseda, T., Hibiya, T., & Shigihara, Y. (2018). Measuring offshore tsunami currents using ship navigation records. *Progress in Earth and Planetary Science*, 5(1), 38. <https://doi.org/10.1186/s40645-018-0194-5>
- Johannessen, J. A., Chapron, B., Collard, F., & Backeberg, B. (2014). *Use of SAR data to Monitor the Greater Agulhas Current* (pp. 251–262). Springer. <https://doi.org/10.1007/978-94-017-8008-7-13>
- Johannessen, J. A., Chapron, B., Collard, F., Kudryavtsev, V., Mouche, A., Akimov, D., & Dagestad, K.-F. (2008). Direct ocean surface velocity measurements from space: Improved quantitative interpretation of Envisat ASAR observations. *Geophysical Research Letters*, 35(22). <https://doi.org/10.1029/2008GL035709>
- Kopsinis, Y., & McLaughlin, S. (2009). Development of emd-based denoising methods inspired by wavelet thresholding. *IEEE Transactions on Signal Processing*, 57(4), 1351–1362. <https://doi.org/10.1109/tsp.2009.2013885>
- Krug, M., Schilperoort, D., Collard, F., Hansen, M. W., & Rouault, M. (2018). Signature of the Agulhas current in high resolution satellite derived wind fields. *Remote Sensing of Environment*, 217, 340–351. <https://doi.org/10.1016/j.rse.2018.08.016>
- Krug, M., & Tournadre, J. (2012). Satellite observations of an annual cycle in the Agulhas current. *Geophysical Research Letters*, 39(15). <https://doi.org/10.1029/2012GL052335>
- Kudryavtsev, V., Myasoedov, A., Chapron, B., Johannessen, J. A., & Collard, F. (2012). Imaging mesoscale upper ocean dynamics using synthetic aperture radar and optical data. *Journal of Geophysical Research*, 117(C4), <https://doi.org/10.1029/2011JC007492>
- Kudryavtsev, V., Yurovskaya, M., Chapron, B., Collard, F., & Donlon, C. (2017a). Sun glitter imagery of surface waves. Part 2: Waves transformation on ocean currents. *Journal of Geophysical Research: Oceans*, 122(2), 1384–1399. <https://doi.org/10.1002/2016JC012426>
- Kudryavtsev, V., Yurovskaya, M., Chapron, B., Collard, F., & Donlon, C. (2017b). Sun glitter imagery of ocean surface waves. Part 1: Directional spectrum retrieval and validation. *Journal of Geophysical Research: Oceans*, 122(2), 1369–1383. <https://doi.org/10.1002/2016JC012425>
- Leber, G. M., Beal, L. M., & Elipot, S. (2017). Wind and current forcing combine to drive strong upwelling in the Agulhas current. *Journal of Physical Oceanography*, 47(1), 123–134. <https://doi.org/10.1175/jpo-d-16-0079.1>
- Le Traon, P. Y., Nadal, F., & Ducet, N. (1998). An improved mapping method of multisatellite altimeter data. *Journal of Atmospheric and Oceanic Technology*, 15(2), 522–534. [https://doi.org/10.1175/1520-0426\(1998\)015<0522:aimmom>2.0.co;2](https://doi.org/10.1175/1520-0426(1998)015<0522:aimmom>2.0.co;2)
- Lumpkin, R., Grodsky, S. A., Centurioni, L., Rio, M.-H., Carton, J. A., & Lee, D. (2013). Removing spurious low-frequency variability in drifter velocities. *Journal of Atmospheric and Oceanic Technology*, 30(2), 353–360. <https://doi.org/10.1175/jtech-d-12-00139.1>
- Lutjeharms, J. R. E. (2007). Three decades of research on the greater Agulhas current. *Ocean Science*, 3(1), 129–147. <https://doi.org/10.5194/os-3-129-2007>
- Lutjeharms, J. R. E., Catzel, R., & Valentine, H. R. (1989). Eddies and other boundary phenomena of the Agulhas current. *Continental Shelf Research*, 9(7), 597–616. [https://doi.org/10.1016/0278-4343\(89\)90032-0](https://doi.org/10.1016/0278-4343(89)90032-0)
- Morrow, R., Fu, L.-L., Arduin, F., Benkiran, M., Chapron, B., Cosme, E., et al. (2019). Global observations of fine-scale ocean surface topography with the surface water and ocean topography (swot) mission. *Frontiers in Marine Science*, 6, 232. <https://doi.org/10.3389/fmars.2019.00232>
- Nencioli, F., Dall’Olmo, G., & Quartly, G. D. (2018). Agulhas ring transport efficiency from combined satellite altimetry and Argo profiles. *Journal of Geophysical Research: Oceans*, 123(8), 5874–5888. <https://doi.org/10.1029/2018JC013909>
- Quilfen, Y., & Chapron, B. (2019). Ocean surface wave-current signatures from satellite altimeter measurements. *Geophysical Research Letters*, 46(0), 253–261. <https://doi.org/10.1029/2018GL081029>
- Quilfen, Y., Yurovskaya, M., Chapron, B., & Arduin, F. (2018). Storm waves focusing and steepening in the Agulhas current: Satellite observations and modeling. *Remote Sensing of Environment*, 216, 561–571. <https://doi.org/10.1016/j.rse.2018.07.020>
- Rasclé, N., Chapron, B., Molemaker, J., Noguier, F., Ocampo-Torres, F. J., Osuna Cañedo, J. P., et al. (2020). Monitoring intense oceanic fronts using sea surface roughness: Satellite, airplane, and in situ comparison. *Journal of Geophysical Research: Oceans*, 125(8), e2019JC015. <https://doi.org/10.1029/2019JC015704>
- Richardson, P. L. (1997). Drifting in the wind: Leeway error in shipdrift data. *Deep Sea Research Part I: Oceanographic Research Papers*, 44(11), 1877–1903. [https://doi.org/10.1016/S0967-0637\(97\)00059-9](https://doi.org/10.1016/S0967-0637(97)00059-9)
- Richardson, P. L., & McKee, T. K. (1984). Average seasonal variation of the Atlantic equatorial currents from historical ship drifts. *Journal of Physical Oceanography*, 14(7), 1226–1238. [https://doi.org/10.1175/1520-0485\(1984\)014<1226:asvota>2.0.co;2](https://doi.org/10.1175/1520-0485(1984)014<1226:asvota>2.0.co;2)
- Richardson, P. L., & Reverdin, G. (1987). Seasonal cycle of velocity in the Atlantic north equatorial countercurrent as measured by surface drifters, current meters, and ship drifts. *Journal of Geophysical Research*, 92(C4), 3691–3708. <https://doi.org/10.1029/jc092ic04p03691>
- Richardson, P. L., & Walsh, D. (1986). Mapping climatological seasonal variations of surface currents in the tropical Atlantic using ship drifts. *Journal of Geophysical Research*, 91(C9), 10537–10550. <https://doi.org/10.1029/JC091iC09p10537>
- Rouault, M. J., Mouche, A., Collard, F., Johannessen, J. A., & Chapron, B. (2010). Mapping the Agulhas current from space: An assessment of ASAR surface current velocities. *Journal of Geophysical Research*, 115(C10), c10026. <https://doi.org/10.1029/2009JC006050>
- Rouault, M. J., & Penven, P. (2011). New perspectives on natal pulses from satellite observations. *Journal of Geophysical Research*, 116(C7). <https://doi.org/10.1029/2010JC006866>
- Tandeo, P., Autret, E., Chapron, B., Fablet, R., & Garello, R. (2014). SST spatial anisotropic covariances from METOP-AVHRR data. *Remote Sensing of Environment*, 141, 144–148. <https://doi.org/10.1016/j.rse.2013.10.024>
- van der Neut, M. (2016). *Eddy tracking with AIS*. Retrieved from http://www.hermess.nl/pdf/Thesis_M.G.vanderNeutRv3.1.1.pdf